REPORT DOCUMENTATION PAGE

Form Approved OMB NO. 0704-0188

1. REPORT DATE (DD-MM-YYYY)	2. REPORT TYPE	3. DATES COVERED (From - To)
25-12-2017	Final Report	11-Aug-2014 - 10-Aug-2017

4. TITLE AND SUBTITLE
Final Report: Microstructural Design of Precipitate Strengthened Alloys with Enhanced Mechanical Properties - Experiments and Simulation

5a. CONTRACT NUMBER
W911NF-14-1-0550

5b. GRANT NUMBER

5c. PROGRAM ELEMENT NUMBER
611102

6. AUTHORS

5d. PROJECT NUMBER

5e. TASK NUMBER

5f. WORK UNIT NUMBER

7. PERFORMING ORGANIZATION NAMES AND ADDRESSES
Arizona State University
ORSPA
P.O. Box 876011
Tempe, AZ 85287 -6011

8. PERFORMING ORGANIZATION REPORT NUMBER

9. SPONSORING/MONITORING AGENCY NAME(S) AND ADDRESS (ES)
U.S. Army Research Office
P.O. Box 12211
Research Triangle Park, NC 27709-2211

10. SPONSOR/MONITOR'S ACRONYM(S)
ARO

11. SPONSOR/MONITOR'S REPORT NUMBER(S)
64036-MS.6

12. DISTRIBUTION AVAILIBILITY STATEMENT
Approved for public release; distribution is unlimited.

13. SUPPLEMENTARY NOTES
The views, opinions and/or findings contained in this report are those of the author(s) and should not contrued as an official Department of the Army position, policy or decision, unless so designated by other documentation.

14. ABSTRACT

15. SUBJECT TERMS

16. SECURITY CLASSIFICATION OF:			17. LIMITATION OF ABSTRACT	15. NUMBER OF PAGES	19a. NAME OF RESPONSIBLE PERSON
a. REPORT	b. ABSTRACT	c. THIS PAGE			Nikhilesh Chawla
UU	UU	UU	UU		19b. TELEPHONE NUMBER 480-965-2402

RPPR Final Report
as of 12-Jun-2018

Agency Code:

Proposal Number: 64036MS **Agreement Number: W911NF-14-1-0550**
INVESTIGATOR(S):

Name: Ph.D. Nikhilesh Chawla
Email: nchawla@asu.edu
Phone Number: 4809652402
Principal: Y

Organization: **Arizona State University**
Address: ORSPA, Tempe, AZ 852876011
Country: USA
DUNS Number: 943360412 EIN: 860196696
Report Date: 10-Nov-2017 Date Received: 25-Dec-2017
Final Report for Period Beginning 11-Aug-2014 and Ending 10-Aug-2017
Title: Microstructural Design of Precipitate Strengthened Alloys with Enhanced Mechanical Properties - Experiments and Simulation
Begin Performance Period: 11-Aug-2014 **End Performance Period:** 10-Aug-2017
Report Term: 0-Other
Submitted By: Ph.D. Nikhilesh Chawla Email: nchawla@asu.edu
Phone: (480) 965-2402
Distribution Statement: 1-Approved for public release; distribution is unlimited.

STEM Degrees: 2 **STEM Participants:** 0

Major Goals: a) Obtain a fundamental understanding of the precise mechanisms for complex dislocation-precipitate interactions.
b) Characterize and quantify morphology of nanoscale theta and theta prime precipitates in three-dimensions nondestructively using Transmission X-Ray Microscopy and understand their evolution and coarsening behavior at high temperatures as a function of time (4D Tomography).
c) Correlate local mechanical behavior of Al-Cu alloys with their 3D microstructure, by means of in situ miniaturized mechanical testing techniques like nanoindentation and micropillar compression.
d) Using a combination of experiments and simulations while also incorporating and analyzing the relevant microstructural features, e.g., precipitate size and spacing, nature of interface, and crystallography, determine the optimum microstructure necessary to obtain desired mechanical properties in model alloys.

Accomplishments: Please see attached PDF.

Training Opportunities: Two graduate students, Shashank Kaira and Ben Gholami, are being trained on this project. A postdoc, Ilaksh Adlakha, has also contributed to simulations in this project.

Results Dissemination: This work has been disseminated at the TMS annual meeting as well as seminars by the PI at universities around the United States.

Honors and Awards: •N. Chawla, Director, Center for 4D Materials Science, ASU.

• N. Chawla, Structural Materials Division Lecture (2017) – The Minerals, Metals, and Materials Society (TMS).

• N. Chawla, Distinguished Alumni Achievement Award (2016) – New Mexico Tech. Recognizes "distinguished alumni who have attained extraordinary distinction in their chosen professional fields and personal endeavors, reflecting well on their education at and affiliation with New Mexico Tech."

• N. Chawla, Structural Materials Division Distinguished Scientist/Engineer Award (2016) – The Minerals, Metals, and Materials Society (TMS).

• N. Chawla, Functional Materials Division Distinguished Scientist/Engineer Award (2016) – The Minerals, Metals, and Materials Society (TMS).

• N. Chawla, Science Award – Environmental Damage in Structural Materials Conference (2016) – Engineering Conferences International (ECI).

Protocol Activity Status:

Technology Transfer: 1. Segmentation using Machine learning (Convolutional neural network method) has been applied on the 3D datasets to allow analysis of ultra-large volumes of material, developed at Argonne National Laboratory.

2. Work in progress to use 3D Finite Element Analysis (OOF) on the Nano-CT datasets, in collaboration with National Institute of Standards and Technology (NIST).

3. Work in progress to use 3D Thermodynamic modeling on the TXM datasets, in collaboration with Dr. Voorhees, from Northwestern University.

4. In situ Mechanical characterization using Micropillar Compression was performed on the Al-Cu alloys, in collaboration with Nanomechanics, Inc.

PARTICIPANTS:

Participant Type: Graduate Student (research assistant)
Participant: C. Shashank Kaira
Person Months Worked: 12.00 **Funding Support:**
Project Contribution:
International Collaboration:
International Travel:
National Academy Member: N
Other Collaborators:

Participant Type: Graduate Student (research assistant)
Participant: Ben Gholami
Person Months Worked: 6.00 **Funding Support:**
Project Contribution:
International Collaboration:
International Travel:
National Academy Member: N
Other Collaborators:

Participant Type: Postdoctoral (scholar, fellow or other postdoctoral position)
Participant: Ilaksh Adlakha
Person Months Worked: 6.00 **Funding Support:**
Project Contribution:
International Collaboration:

RPPR Final Report
as of 12-Jun-2018

International Travel:
National Academy Member: N
Other Collaborators:

DISSERTATIONS:

Publication Type: Thesis or Dissertation
Institution: Arizona State University
Date Received: Completion Date:
Title: Structure-Property Relationships in Aluminum-Copper alloys using Transmission X-Ray Microscopy (TXM) and Micromechanical Testing
Authors: C. Shashank Kaira
Acknowledged Federal Support: **Y**

Contract Information

Contract Number	W911NF1410550
Title of Research	Microstructural Design of Precipitate-Strengthened Alloys with Enhanced Mechanical Properties – Experiments and Simulation
Principal Investigators	N. Chawla and K. Solanki
Graduate Students	C. Kaira, I. Adlakha, B. Gholami Bazehhour
Organization	Arizona State University

Technical Section

Technical Objectives

a) Obtain a fundamental understanding of the precise mechanisms for complex dislocation-precipitate interactions.

b) Characterize and quantify morphology of nanoscale θ′ and θ precipitates in three-dimensions non-destructively using Transmission X-Ray Microscopy and understand their evolution and coarsening behavior at high temperatures as a function of time (4D Tomography).

c) Correlate local mechanical behavior of Al-Cu alloys with their 3D microstructure, by means of *in situ* miniaturized mechanical testing techniques like nanoindentation and micropillar compression.

d) Using a combination of experiments and simulations while also incorporating and analyzing *the relevant microstructural features, e.g., precipitate size and spacing, nature of interface, and crystallography*, determine the optimum microstructure necessary to obtain desired mechanical properties in model alloys.

Technical Approach

Precipitation-strengthened alloys, such as Al-Cu alloys are ubiquitously used in almost all structural applications and their superior mechanical performance can be attributed to the complex distribution of second phase intermetallic particles that precipitate out from the alloy's solid solution matrix. These precipitates are the primary strength imparting components of the alloy and they do so by serving as obstacles to dislocation motion. The mechanical behavior of these precipitate-strengthened alloys, is controlled by the nature of the particle/matrix interface,

particle size, and subsequent dislocation-particle interactions [1]. If the precipitates are fine and coherent, precipitate shearing takes place. However, in the overaged condition, the particles are larger and incoherent with the matrix, so the dislocation attempts to by-pass the precipitate. Analytical solutions exist that correlate, for example, the stress to bypass the dislocation with the spacing between particles (λ) [2]. Experimental verification of these models is very difficult because the models assume very idealistic conditions, i.e., no variability between size and spacing of particles, a single slip plane, etc. More importantly, the bulk alloy consists of a heterogeneous microstructure, implying that different regions of the material may have varying particle size, spacing, and even grain crystal structures. It is necessary to be able to conduct experiments on volumes with controlled particle size and spacing. Furthermore, it is necessary to characterize the microstructure in these volumes non-destructively and to quantify the evolution of this structure during deformation non-destructively.

Atomistic, discrete dislocation, and crystal plasticity frameworks can reveal a coupled relationship between the incipient dislocation interactions and key parameters, such as the precipitate character (size and spacing), to the material hardening behavior. Atomistic tools have been used primarily to study strengthening due to coherent precipitates [3], mechanisms associated with void and precipitate strengthening in alpha-iron [4], precipitate-size effect on the dislocation core structure [5], and interaction of screw dislocations with Guinier-Preston (GP) zones [6]. Similarly, discrete dislocation dynamics has been employed to reveal the effect of solute friction on dislocation-dislocation interactions [7], the role of dislocation character on bypass and pinning mechanisms [8], and the effect of source and obstacle strengths on yield stress [9]. In summary, although these studies reconfirmed many classical theories pertaining to solute strengthening, several unresolved questions remain, particularly those related to the specific strengthening mechanisms in these alloys and the effect of microstructural length scales (particle spacing, size, interface coherency, etc.) on the control of macroscopic flow stress. In this work, we employ atomistic simulations to examine various scenarios of dislocation-precipitate interactions. Overall, this work aims to provide insights for improving continuum and discrete dislocation attempts to model precipitate hardened materials. Therefore, the critical resolved shear stress, τ_c is quantified across several scenarios.

The pressing need to have more precise models of structure-property relationships calls for the need to have a detailed understanding of the microstructure. For this purpose, non-destructive

3D microstructural characterization as well as *in situ* mechanical testing (4D Characterization) has been carried out using the new Transmission X-ray Microscope (TXM) of the Advanced Photon Source (APS) at sector 32-ID-C in Argonne National Laboratory, to perform absorption full-field nano-computed tomography (nano-CT) at a spatial resolution of sub-60 nm.

Experimental methods

The schematic of the Transmission X-ray Microscope is shown in Figure 1(e). A monochromatic beam at 9 keV was utilized to acquire 2D projections. Choice of beam energy (9.1 keV) was made from the contrast between the two phases (beyond Cu *K-edge* at 8.96 keV) in the X-ray mass attenuation co-efficient plot. A single-capillary optic with a diameter of 435 μm (beam acceptance of 0.097 mm^2) developed at Cornell University, was used as the condenser to focus X-rays onto the sample. The condenser divergence matches the numerical aperture of a 180 μm large Fresnel zone plate with 60 nm outer most zone width, which was used as a microscope objective lens to magnify radiographs of the sample placed on a high accuracy air-bearing rotary stage. A magnification of ~47 was obtained with the distance between the CCD and sample set to 3.4 m. The X-ray detection system comprised of an assembly of a LuAG scintillator, a 10X microscope objective, a 45^o mirror and a low-noise fast CCD cooled at -40 ^oC. The field of view was about 30 x 40 μm^2 in this geometry and a voxel width of 16.6 nm was achieved, while the illumination coming from the beam-shaping condenser (BSC) was a disk slightly larger than 70 μm. 3D reconstructions were performed using the software Tomopy, an open source Python based toolbox used to analyze synchrotron tomography data. The stack of tomograms thus obtained were then carefully processed in ImageJ using a series of different filters to reduce artifacts and noise. This enabled smoother segmentation of precipitates, which was performed in 3D using Avizo® Fire.

99.999% pure Al-4wt.% Cu samples in wire form (0.5 mm diameter) were solutionized for 24 hours at 535 ^oC to ensure presence of large grains and subsequently aged at two different temperatures, 350 ^oC and 400 ^oC, to study precipitate evolution. Choice of such high aging temperatures restricted our study mainly to the θ′ and θ precipitates. The straightened wires were mechanically polished carefully to a sharp tip, so as to fit in the microscope's field of view. The relatively low X-ray energies utilized also restricts the thickness of the sample that can be

analyzed. Due to the instrument's limited depth of field too, micropillars roughly 20 μm in diameter and 40 μm in length were fabricated at the tips of sharpened wires using a dual-beam Zeiss® Auriga focused ion beam (FIB) workstation, as shown in Figure 1(a). For post-scanning analysis using EBSD, the tips of the samples were cross-sectioned using the FIB at an accelerating voltage of 30 keV and using a current of 1 nA. EBSD was performed on these flat sections, using a step size of 0.5 μm to identify the grain orientation of the α-Al matrix. TSL® OIM data collection and analysis software was used to analyze the acquired EBSD data.

Al-4wt.%Cu wire samples were mounted and polished flat metallographically up to a 0.05 μm colloidal silica finish and subsequently used for microscale testing. These samples were solution treated for long times to ensure large grain sizes, so as to eliminate any heterogeneity arising from crystallographic orientation. The micromechanical testing route included fabrication of micropillars (4 μm x 12 μm) on a particular grain, uniaxial compression of these pillars followed by heating the sample at 350 ^{o}C to resume the aging process and repeat the above procedure for different aging times. This was performed to obtain the variation in stress-strain response for different aging times. A Ga^{+} ion beam, at an accelerating voltage of 30 keV, was used at a range of currents, starting with 16 nA to mill out a trench to provide clearance for the nanoindenter's flat punch tip, leaving behind a coarse pillar of about 10 μm in diameter. The size of the coarse pillar was then reduced using currents of 4 nA and 1 nA. Subsequent final thinning was performed at 0.1 nA. The final milling step using a fine current ensured the minimization of taper ($<2^{o}$) and also minimized the damage that could prevail from the use of the Ga^{+} ion beam. A thin layer of platinum deposited using EBID (Electron beam-induced deposition) prior to milling also ensured minimization of taper and rounding at the micropillar's top surface. The size of the pillars were intentionally chosen to be quite large, so as to avoid any effects of Ga^{+} damage on mechanical properties, caused due to FIB milling. It was also ensured that the size of the pillars chosen were representative of the bulk microstructure. Fabrication using the annular milling technique ensured Ga^{+} ion impact with only grazing incidence. The size of the damage layer on either side was quantified using a TEM specimen of a micropillar's cross-section. This damaged amorphous layer at the surface was found to be relatively small (~8 nm). Accounting for the size of the micropillars, it can be safely concluded that the damage layer from grazing incidence of the Ga^{+} beam will have minimal impact on the mechanical properties measured using micropillar compression.

Micropillar compression was performed using a commercial Nanoindenter (XP, Agilent Technologies, AZ) using a diamond indenter tip with a flat square cross-section (10 µm x10 µm). A cyanoacrylate based adhesive was used to mount the sample onto an aluminum stub. A constant displacement rate of 7 nm/s was used to maintain a nominal strain rate of ~10^{-3} s^{-1}. The experiments were initiated when the thermal drift fluctuations reduced to a value below 0.05 nm/s. The top diameter of the micropillars was used for the calculation of stress. The post-deformed pillars were analyzed at a 35^{o} tilt using scanning electron microscopy (SEM).

To observe the interaction of dislocations with the nanoscale precipitates, a TEM sample was prepared using the standard FIB lift-out technique. A representative micropillar at the initial aging condition (t= 45 mins), compressed to its yield point, was used for this purpose. TEM investigation was performed in an aberration-corrected FEI 80-300 Titan™ operated at 300 kV. NanoFlip, an *in situ* Nanoindenter (Nanomechanics, Inc., Knoxville, Tennessee) was installed in the dual-beam Zeiss® Auriga focused ion beam (FIB) workstation to carry out *in situ* micropillar compression.

To further understand their mechanical behavior and the evolution of damage *in situ* in 3D, a compact Nanoindentation system was designed to carry out micropillar compression at regular intervals post-scanning at the Transmission X-ray Microscope (TXM) of the Advanced Photon Source (APS) at sector 32-ID-C in Argonne National Laboratory.

Experimental results

4D Microstructural characterization using Nano-CT at 350 ^{o}C

The wire samples were scanned about their longitudinal axis. Presence of large grains ensured that the study of evolution was restricted to within a single grain. Transmission X-ray Microscopy allowed characterization of the same volume of nanoscale precipitates during evolution. Z-projection tomogram obtained after 3D reconstruction has been shown in Figure 1(c). Accurate 3D measurements of length, thickness, aspect ratio and precipitate shape can be made using these results. For several decades, experimental measurements have been made using transmission electron microscopy to understand the thickening and lengthening kinetics of precipitates and reconcile these observations with various theories but however, precise measurements have not been possible due to the destructive as well as 2D nature of this

technique. There is also quite some disagreement regarding the growth rate exponent for thickening & lengthening and the size-distribution plots do not seem to conform exactly to theoretical predictions. Such discrepancies can be overcome with nano-computed tomography, which serves as a new paradigm to answer these fundamental questions.

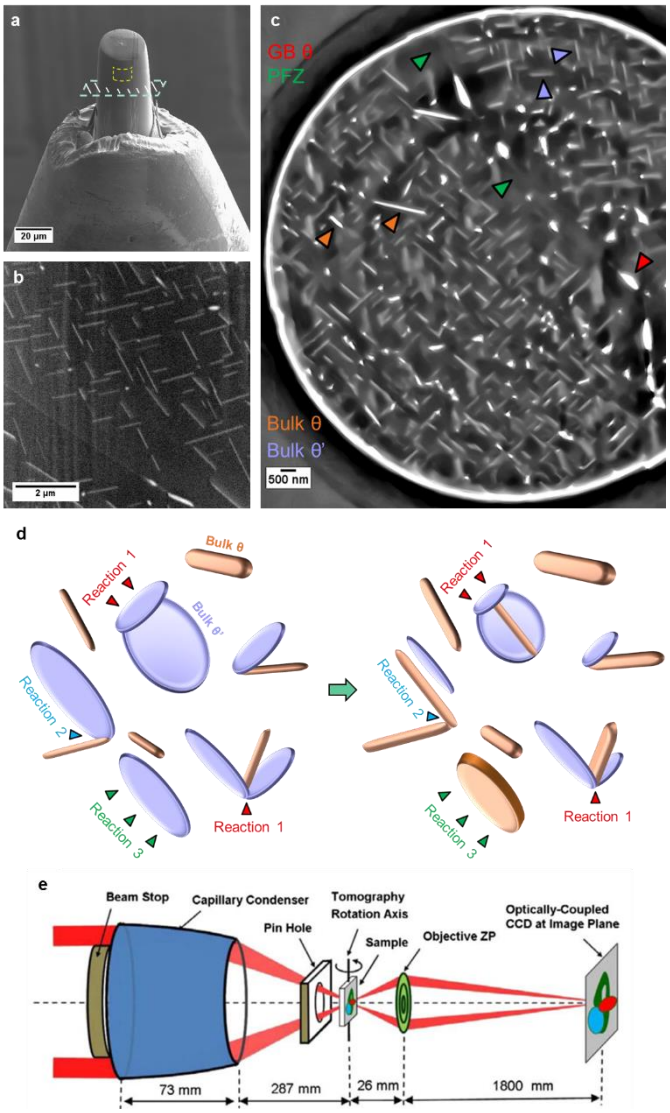

Figure 1: (a) SEM micrograph showing a micropillar (30 µm x 50 µm) fabricated at the tip of Al-4wt.%Cu wire. (b) SEM micrograph showing a magnified view of the micropillar's surface (shown in a) where precipitates as well as a grain boundary are visible. (c) 2D slice from a reconstructed dataset (T=350 ^{o}C, t=45 mins) showing a cross-sectional plane of view (depicted in a) from within the micropillar. The grain boundary, different phases (θ′ and θ) as well as the precipitate free zone (PFZ) have been highlighted. (d) Schematic illustrating the different transformation reactions occurring in the bulk during aging at 350 ^{o}C. (e) Schematic of the TXM used for 3D characterization at APS [10].

A spatial resolution of 60 nm on the TXM ensured that the θ′ precipitate morphology could be captured in its early stages, where they assume a plate-like shape. A motley of precipitate sizes and shapes were observed in the Al-Cu alloy aged at 350 ^{o}C. Combination of different morphologies of precipitates can also be seen to coalesce. The θ′ precipitates primarily exist as

orthogonally oriented plates, while the θ precipitates are more needle/lath-like and randomly oriented. Figure 2 shows the 3D rendering of the microstructure for different aging times from a region sampled near a grain boundary in the scanned micropillar. The Volume fraction of θ′ was seen to reduce and that of θ increased. The 3D tomography data allowed us to visualize these bulk transformation reactions.

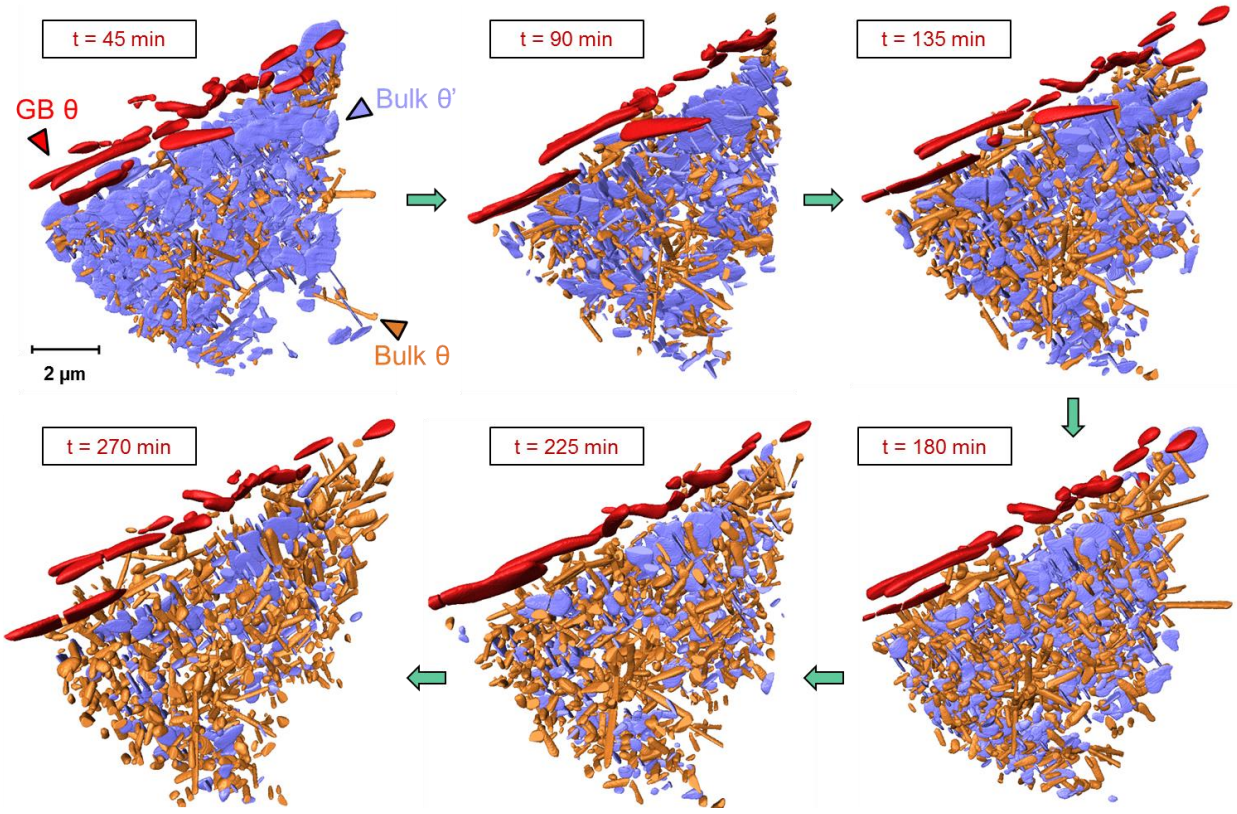

Figure 2: 4D Microstructural characterization at 350 ^{o}C. 3D rendering of microstructural evolution (of θ′ and θ) with aging time has been depicted. The volume fraction of θ is seen to increase while that of θ′ decreases. Heterogeneously nucleated θ phase at the GB (grain boundary) has been shown in red.

Laird and Aaronson [11] were able to observe some of the transformation sequences occurring in an Al-Cu alloy using a hot-stage specimen holder in a TEM. But the true nature of these transformations were masked due to the foil nature of the specimen, as interaction on only a single plane of view was captured. For instance, one of the most commonly observed reactions in

their study was the dissolution of θ′ and the growth of θ without actual contact but by countercurrent diffusion of aluminum and copper through the α matrix. However, our study has been able to show otherwise. Although diffusion through the matrix does play a role in dissolution and growth of precipitates, θ is generally seen to nucleate and grow from θ′- θ′ or θ′- θ intersections and this can be easily missed when viewed in 2D due to the precipitate's complex morphology. The nucleation of θ was most commonly seen to occur at θ′- θ′ intersections (Reaction 1) and its growth occurred at the expense of these θ′ plates, eventually causing them to split up and shrink. This can have a key impact on the alloy's mechanical properties due to a transition in the interfacial structure of precipitates (θ′ to θ) and the precipitate density. Less commonly, θ was also seen to nucleate from θ′- θ intersections (Reaction 2) and a smaller proportion of θ′ plates directly transformed into morphologically similar θ plates (Reaction 3). Another important observation is the dissimilarity in dissolution/growth rates of individual precipitates. This highlights the heterogeneity in diffusional interactions, which is a direct result of the local spatial distribution of precipitates.

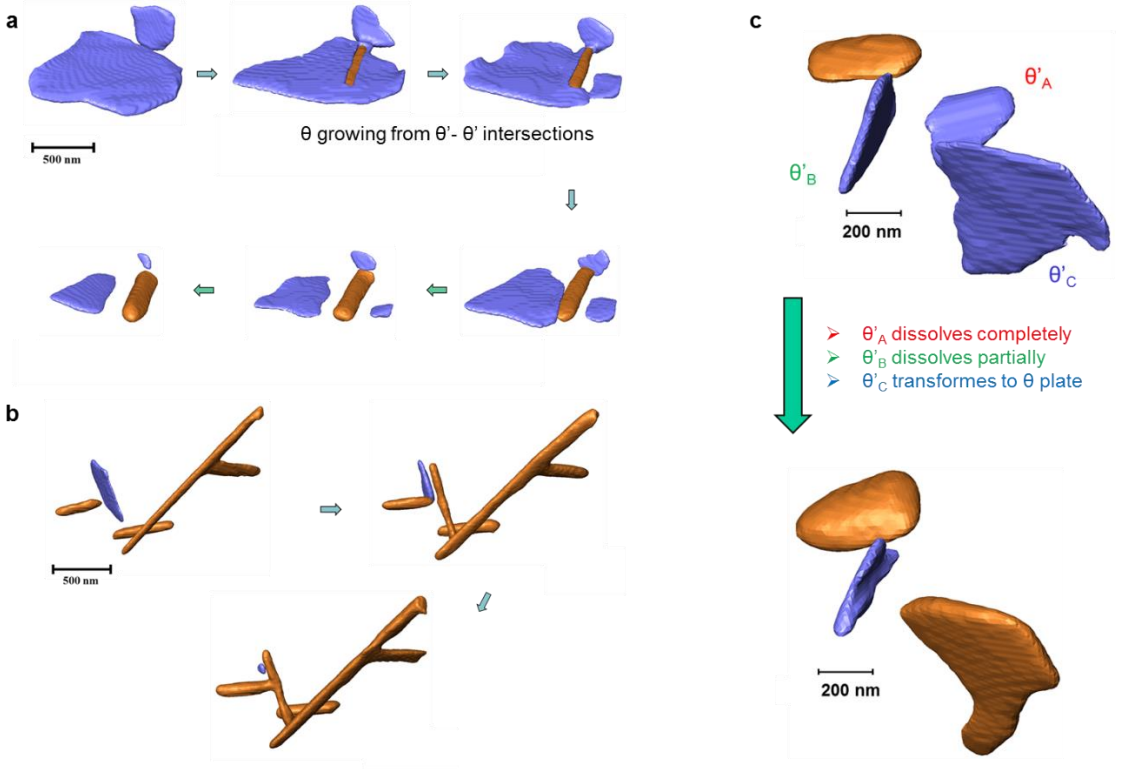

Figure 3: 3D rendering of different transformation reactions (θ′ to θ) occurring during aging at 350 ^{o}C. (a) Nucleation and growth of θ from θ′- θ′ intersection. (b) Nucleation and growth of θ from θ′- θ intersection. (c) Varying dissolution rates of different θ′ precipitates.

The unique ability to measure and track an individual precipitate's dimensions in 3D also allowed us to estimate the bulk diffusion coefficient (D_{bulk}) of Cu in Al, by employing the Zener-Hillert expression[12], [13],

$$\frac{vR_{tip}}{D_{bulk}} = \frac{(X_{bulk} - X_{eq}^{\alpha/\theta})}{2(X_{\theta} - X_{eq}^{\alpha/\theta})}\left(1 - \frac{R_c}{R_{tip}}\right) \quad (1)$$

where R_{tip} is tip radius of the θ needle (~half of its width), v is its growth velocity, R_c is the critical radius of curvature (which can be assumed to be $0.5R_{tip}$ [12], [13]), X_{bulk} is the bulk Cu concentration in the alloy, $X_{eq}^{\alpha/\theta}$ is the equilibrium concentration of Cu at the α/θ interface and X_{θ} is the concentration of Cu in θ phase. D_{bulk} was found to be on the order of 10^{-16} m^2/s, which is again in excellent agreement with values computed using other techniques [14]. It must also be noted that lengthening rates measured in the TEM yielded diffusivity values [11], [15] on the order of 10^{-14} m^2/s, where an obvious influence of surface diffusion is apparent.

4D Microstructural characterization using Nano-CT at 400 ^{o}C

Coarsening has been widely observed in a variety of particle-dispersed systems, where the system strives to attain thermodynamic stability by minimizing the total surface energy of the ensemble. The LSW theory, put forth by Lifshitz and Slyozov [16] and Wagner [17], has been able to explain the diffusion-controlled Ostwald ripening process in great mathematical detail. It predicts the kinetics of the coarsening process (where mean radius of the particles obey a cubic growth law) and the scaled precipitate size distributions (PSDs) to be time invariant. However, application of this theory on metallic systems has been largely debated since its inception and hence, several modifications [18]–[20] were put forth that were able to better address the misfit between experiments and theory. It must also be noted that most of these studies focused on modifying the LSW theory to account for the apparent deviation, while little attention has been paid to the experimental techniques used to validate the theory. It can be stereographically quite challenging and sometimes nearly impossible to extract accurate particle dimensions from 2D

Images, especially with particles having complex morphologies. This can give rise to inaccurate size-distribution curves, which are crucial in discerning the rate-controlling diffusion mechanism during coarsening. Most studies on Al-Cu alloys have found the experimental size-distribution curves to be broader when compared to their theoretical counterparts and various factors such as overlap of the particle's diffusion fields, coalescence, misfit strains, etc. have been attributed to this finding [21]–[23]. There has also been evident lack of common ground in the observed lengthening and thickening rates of these precipitates [24], which subsequently causes uncertainty in discerning the rate-controlling diffusion mechanism. These experimental shortcomings have been overcome using X-ray Nano-CT, where it has been possible to sample a statistically large volume and extract three-dimensional information such as 3D orientation, 3D volume, 3D surface area and maximum and minimum feret diameter from all individual particles. The Al-4wt.% Cu alloy was aged at 400 ^{o}C to closely monitor the coarsening of the θ phase alone (Figure 4).

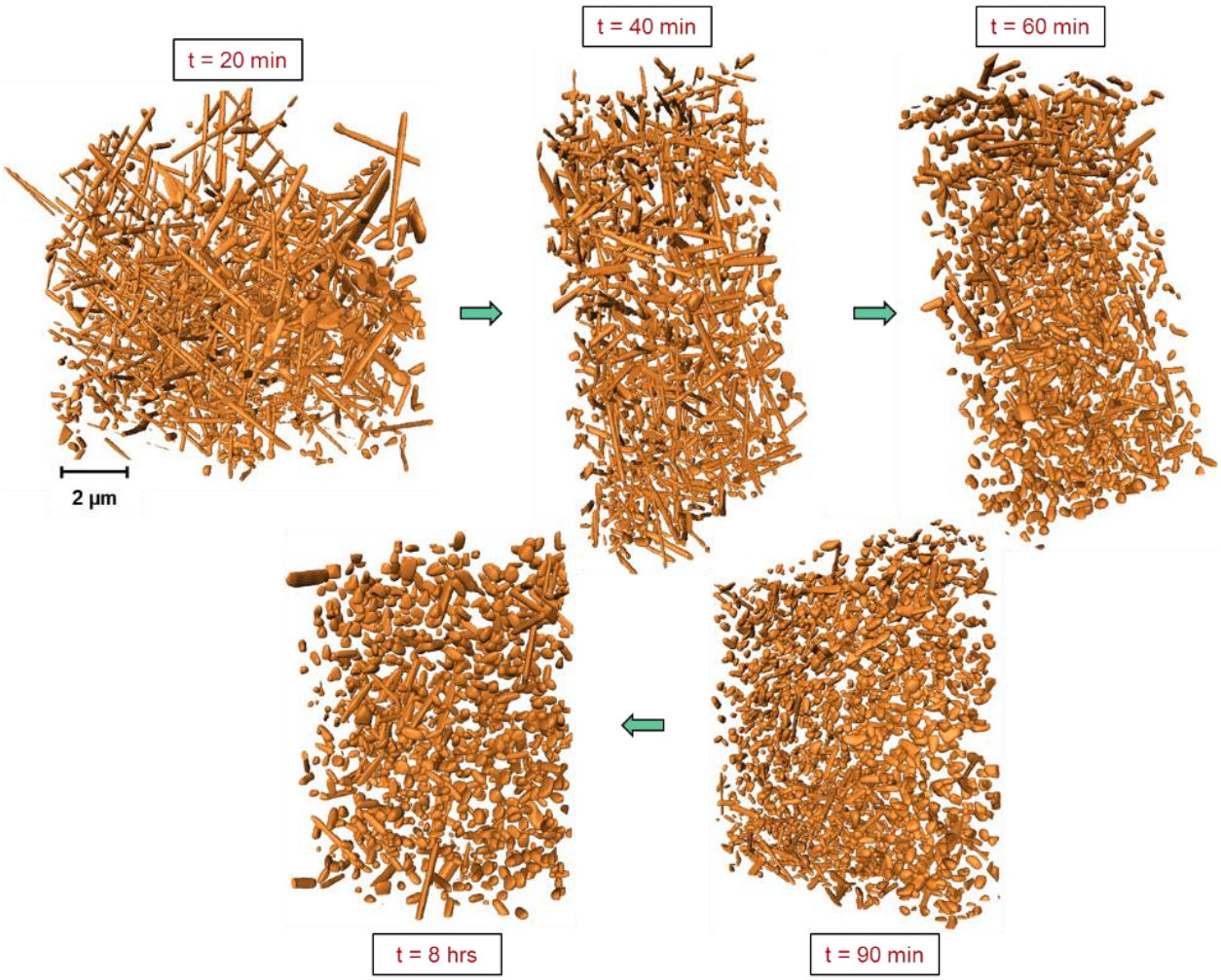

Figure 4: 4D Microstructural characterization at 400 ^{o}C. 3D rendering of microstructural evolution (of θ) with aging time has been depicted. The aspect ratio of the θ precipitates continually reduces.

The Sauter Mean Diameter was calculated for the entire assembly of precipitates and its mean value was seen to be in good agreement with both the power laws D_m^2 vs. t and D_m^3 vs. t. The PSDs obtained using the Sauter Mean Diameter were initially broad and seem to transition to better conformity with the PSD theoretically predicted by the LSW theory.

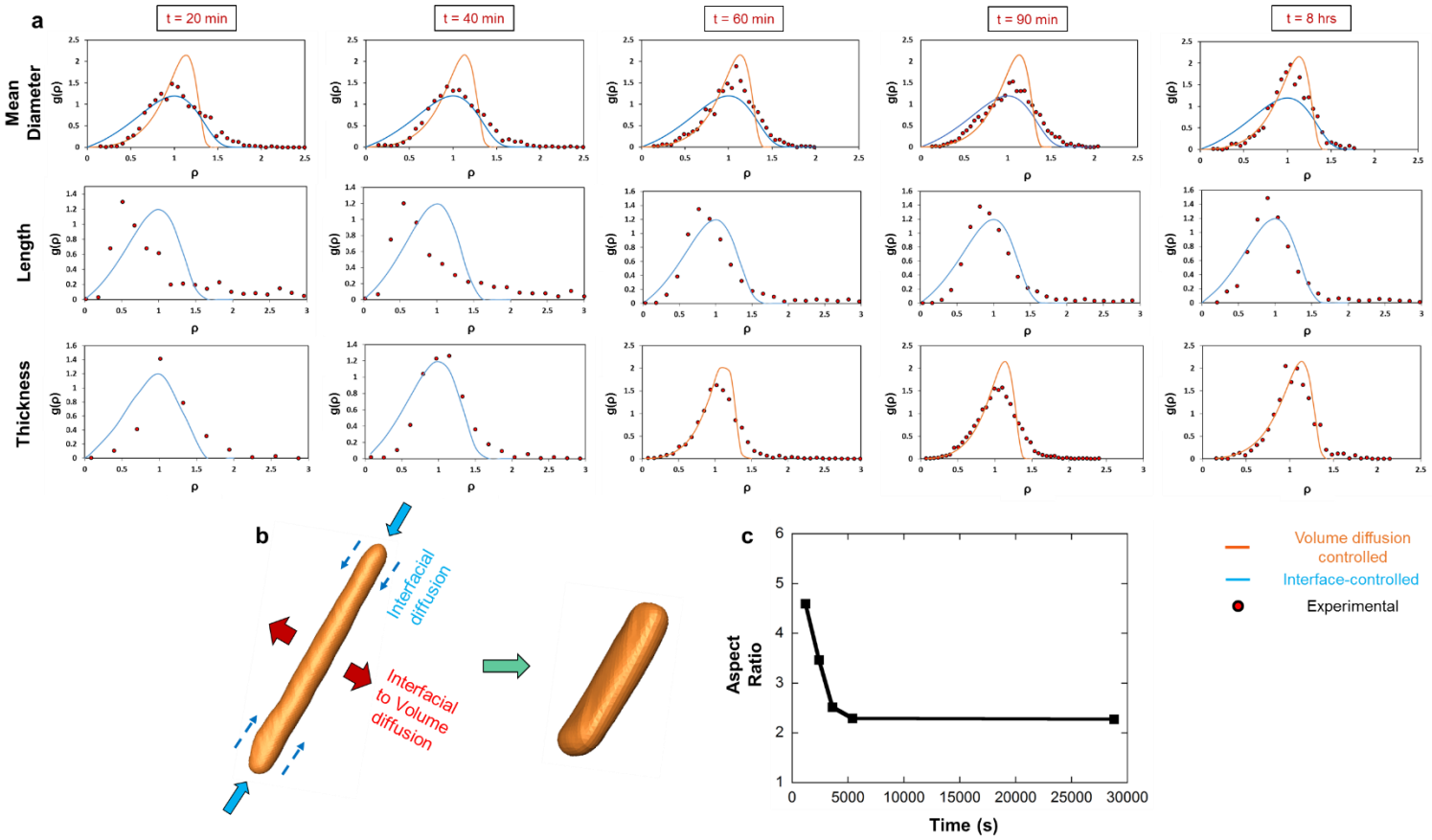

Figure 5: (a) Length, thickness and mean diameter PSD curves have been plotted for all aging times (T=400 ^{o}C) and the corresponding theoretical PSDs for Volume diffusion controlled and Interface controlled processes have been shown. The vertical axis represents the scaled probability density g(ρ) while ρ represents the scaled particle dimensions. The growth in thickness of θ is initially interfacially driven but later switches to volume diffusion controlled growth as the interfaces lose coherency. The reduction in length is always controlled by interfacial diffusion (b) Schematic representing the transformation of θ phase (c) Quantification of reduction in aspect ratio of θ during aging.

The growth exponent as well as the scaled PSDs (Figure 5) hint towards the possibility of both volume-diffusion as well as interface-controlled diffusive processes being operative. This hypothesis was validated by constructing separate scaled PSD curves for both length and thickness of the precipitates, respectively. The thickening of the θ phase is initially driven by

interface-controlled growth due to the semi-coherent nature of its broad faces (as corroborated by observation of ledges in Kang and Laird's study [25]), but later switches to volume diffusion controlled growth as its interfaces lose coherency. The length of these precipitates on the other hand, continually reduce by interface-driven diffusion, suggesting the diffusion of solute from the extremities along the periphery. The coarsening of the θ phase is seen to manifest primarily as an evolution of its shape to an equilibrium morphology. Although several theories predict broadening in the PSD curves as a result of volume fraction, it is possible that its role has been overstated as exemplified by our 3D measurements.

3D Orientation Information

Another successful advancement in this study is the correlation of nanotomography data and Electron backscatter diffraction (EBSD) data to obtain 3D crystallographic orientation information. The tips of the scanned samples (aged at 400 ^{o}C) were cross-sectioned normal to the scanning axis by making use of the focused ion beam (FIB). EBSD data acquired from the flat section was used to determine the crystallographic orientation of the α Al matrix. The grain sizes of the samples under study were quite large (~400 μm) and hence, data gathered from both the techniques were used to complement each other as they corresponded to a single grain. Miller indices of the plane normal to the scanning axis were utilized to transform the coordinate axes of the sample in 3D to correspond to the crystallographic axes of Al. The orientation of the maximum feret diameter of the precipitates obtained in three-dimensional space using Avizo® was utilized to construct stereographic pole figure maps (Figure 6(c)). This novel approach furthered our understanding of the preferred orientation that these elongated θ precipitates possess in 3D. It is evident from the (100) pole figure map that the θ phase primarily tends to be oriented along the <100> cubic axes of the α Al matrix phase.

After transforming the coordinate axes of the 3D dataset, it was also possible to re-section the virtual microstructure on any particular crystallographic plane using Avizo®. This can play a pivotal role in understanding the mechanical properties of the alloy. Deformation in metallic systems primarily occurs through slip on specific planes and hence, determining the distribution of precipitates on these planes is paramount to gauging the strengthening that these precipitates cause. The version of the Orowan equation [26], [27] which has been used to describe strengthening ($\Delta\tau_p$) caused by shear-resistant particles is given by

$$\Delta\tau_{p3D} = \frac{Gb}{2\pi\lambda\sqrt{(1-v)}} ln\left(\frac{D_p}{r_o}\right) \quad (2)$$

where G is the shear modulus of the aluminum matrix, v is Poisson's ratio, λ is the planar inter-particle spacing, D_p is mean planar particle diameter, r_o is the outer cut-off radius for matrix dislocations and b is the magnitude of the burgers vector of these dislocations.

Up until now, mathematical simplifications were used to modify this equation to account for the non-spherical nature of precipitates [27]. However, our ability to measure the inter-particle spacing λ and mean diameter D_p of the precipitates on glide planes (Figure 6(b)) has allowed experimental estimation of the Orowan stress. Histogram of spacings is shown in Figure 6(d). Figure 6(e) shows the variation of the increment in the critical resolved shear stress (CRSS) caused by Orowan strengthening (Δτ). The version of the Orowan equation that uses λ_{eff} to describe strengthening caused by $<100>_\alpha$ rods [28], which is applicable in the current case, is given by

$$\Delta\tau_{p2D} = \frac{Gb}{2\pi\sqrt{(1-v)}}\left\{\frac{1}{\left(1.075\sqrt{0.433\pi/f} - \sqrt{1.732}\right)d_t}\right\} ln\left(\frac{\sqrt{1.732}\, d_t}{r_o}\right) \quad (3)$$

where f is the volume fraction of the strengthening phase and d_t is the mean diameter of the rods. This equation, however, can be quite misleading, as in the current scenario due to multiple modes of deformation operating. Previous studies on this system have shown Orowan looping to be operative at inter-particle spacings below 0.5 μm, beyond which the self-trapping tendency of dislocations becomes dominant and dislocation cell-structures are formed between precipitates [29]. However, our ability to measure inter-particle spacings and mean diameter D_p of the precipitates on all glide planes (Figure 6b) in 3D has allowed experimental estimation of the increment in the critical resolved shear stress (CRSS) caused by Orowan strengthening ($\Delta\tau_p$). A comparison has been made with Orowan strengthening values estimated from the 2D analytical model using Equation (3). A stark difference is seen in both the trend as well as the strengthening values.

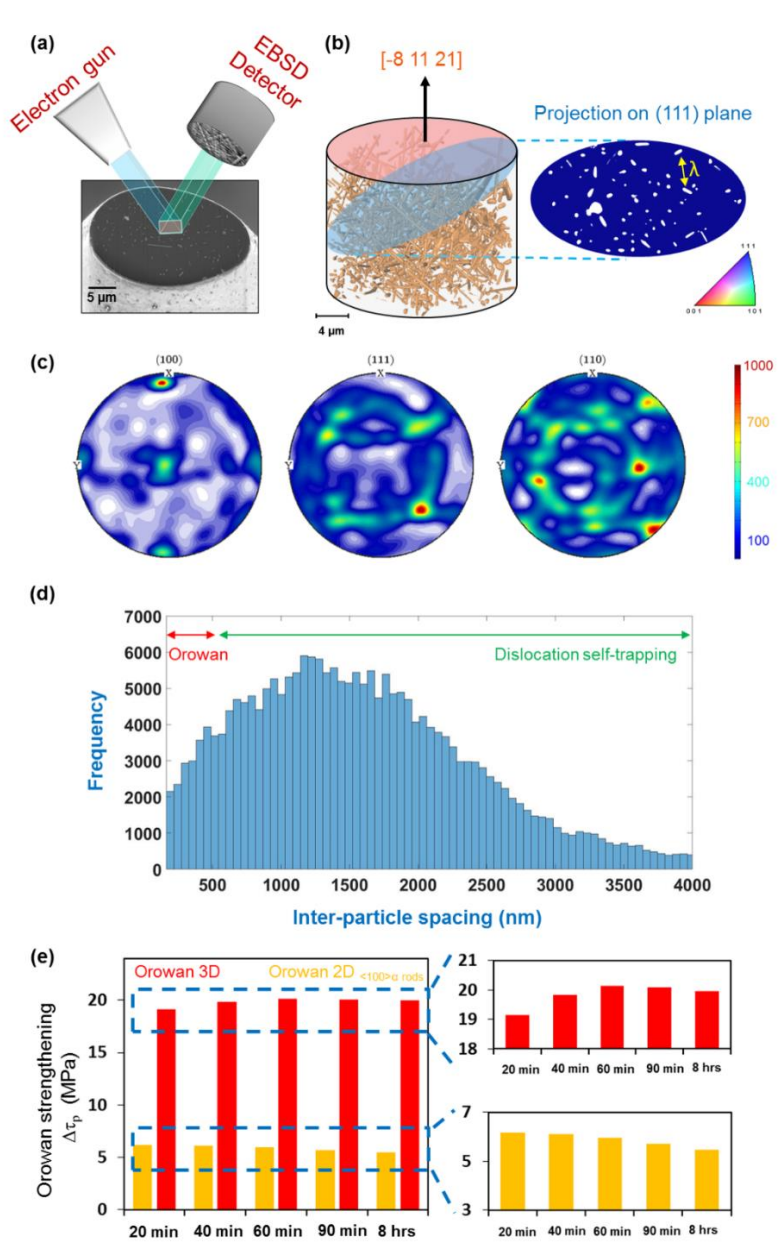

Figure 6: 3D Orientation Information (a) Acquisition of EBSD data from FIB cross-sectioned top surface of the Al-4wt.%Cu wire aged to 400 ^{o}C (b) Schematic showing re-sectioning of the virtual microstructure to obtain inter-particle spacing (λ) from the (111) slip plane (c) Pole figure maps representing the 3D crystallographic orientation of the maximum Feret diameter of the θ precipitates. The legend represents the number of precipitates. (d) Frequency distribution of inter-particle spacings between θ precipitates on all (111) planes of the microstructure. (e) Comparison of the increment in CRSS caused by Orowan strengthening ($\Delta\tau_p$) estimated both from 3D data and the 2D analytical model (using Equation (3)), as a function of aging time.

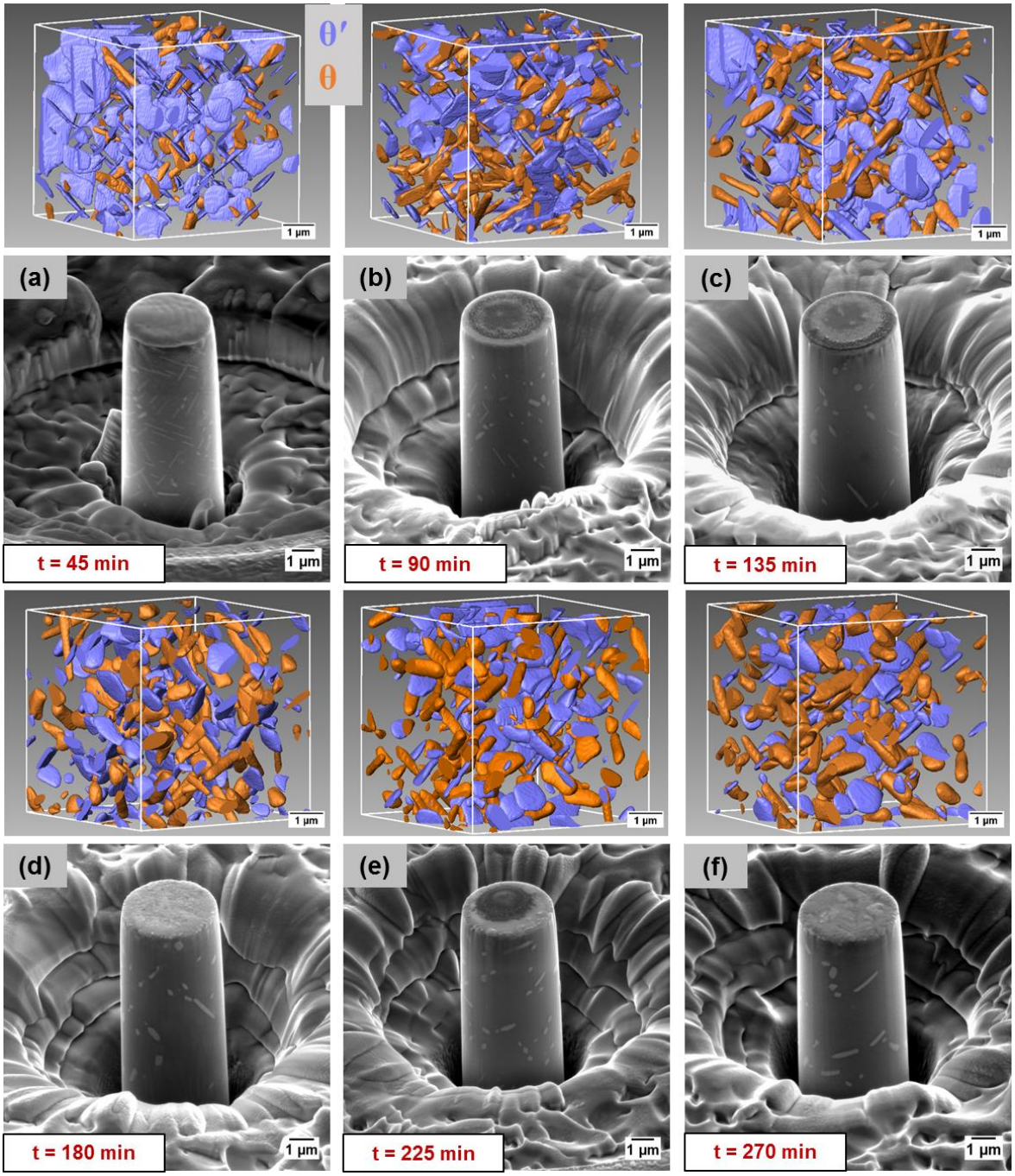

Figure 7: Scanning electron microscope (SEM) images showing representative micropillars fabricated in a single grain at different aging times (T = 350 ^{o}C). Corresponding 3D rendition of the microstructure from Transmission X-ray Microscopy (TXM) for each aging condition has also been displayed.

Transition in Deformation Behavior upon Aging using Micropillar Compression

The Micropillar compression tests were limited to samples aged at 350 ^{o}C. At each aging condition, four micropillars were fabricated and tested (summing up to a total of 24 micropillars), to provide statistically relevant mechanical data. The onset of plasticity in case of micropillars can be quite a stochastic process and hence, a larger number of tests can help reduce uncertainty in determining the yield stress. Compression of these micropillars (shown in Figure 7) yielded stress-strain curves that were marked by numerous strain bursts. A representative stress-strain curve has been shown in Figure 8(a). Initial plasticity is marked by small such bursts which correspond to either local avalanches of groups of dislocations or shearing of individual θ′ precipitates, while the larger bursts correspond to slip bands propagating through the volume of the micropillar. These bursts can have different origins in different materials. Although in this study, this was corroborated by *in situ* micropillar compression experiments (Figure 9), which enabled direct correlation of stress-strain data with live shearing events occurring during deformation of the micropillar. Similar micropillar compression experiments were performed on 99.999% pure Al samples (Princeton Scientific Corp., Easton, PA, USA), to serve as a comparison and to "back out" the effect of the Al matrix on the deformation behavior. The fracture behavior of these single-crystalline micropillars was found to be significantly different, where a few large strain bursts occurred (corresponding to shear bands causing fine slip in the micropillar) with minimal strain hardening (Figure 8(b)).

After the onset of plasticity, the deformation behavior transitions significantly as a function of aging time. Strain bursts in the stress-strain curves correspond to shearing events at initial aging conditions. Upon aging, these bursts correspond mainly to dislocation avalanches between shear-resistant θ precipitates. Figure 8(c) clearly depicts multiple slip bands shearing an individual θ′ precipitate, as seen from the surface of the micropillar. Transition from planar slip to wavy slip is seen at t= 90 mins (Figure 8(d)). As the volume fraction of shear-resistant θ gradually increases, the propensity to cross-slip in Al alloys promotes deformation through wavy slip. A stark transition is seen at later aging conditions, where the soft Al matrix plastically flows around the shear-resistant θ precipitates (t= 180 mins, Figure 8(e)). At t= 270 mins (Figure 8(f)), voids are seen to form at the interfaces of θ precipitates as a result of severe strain incompatibilities resulting in interfacial failure.

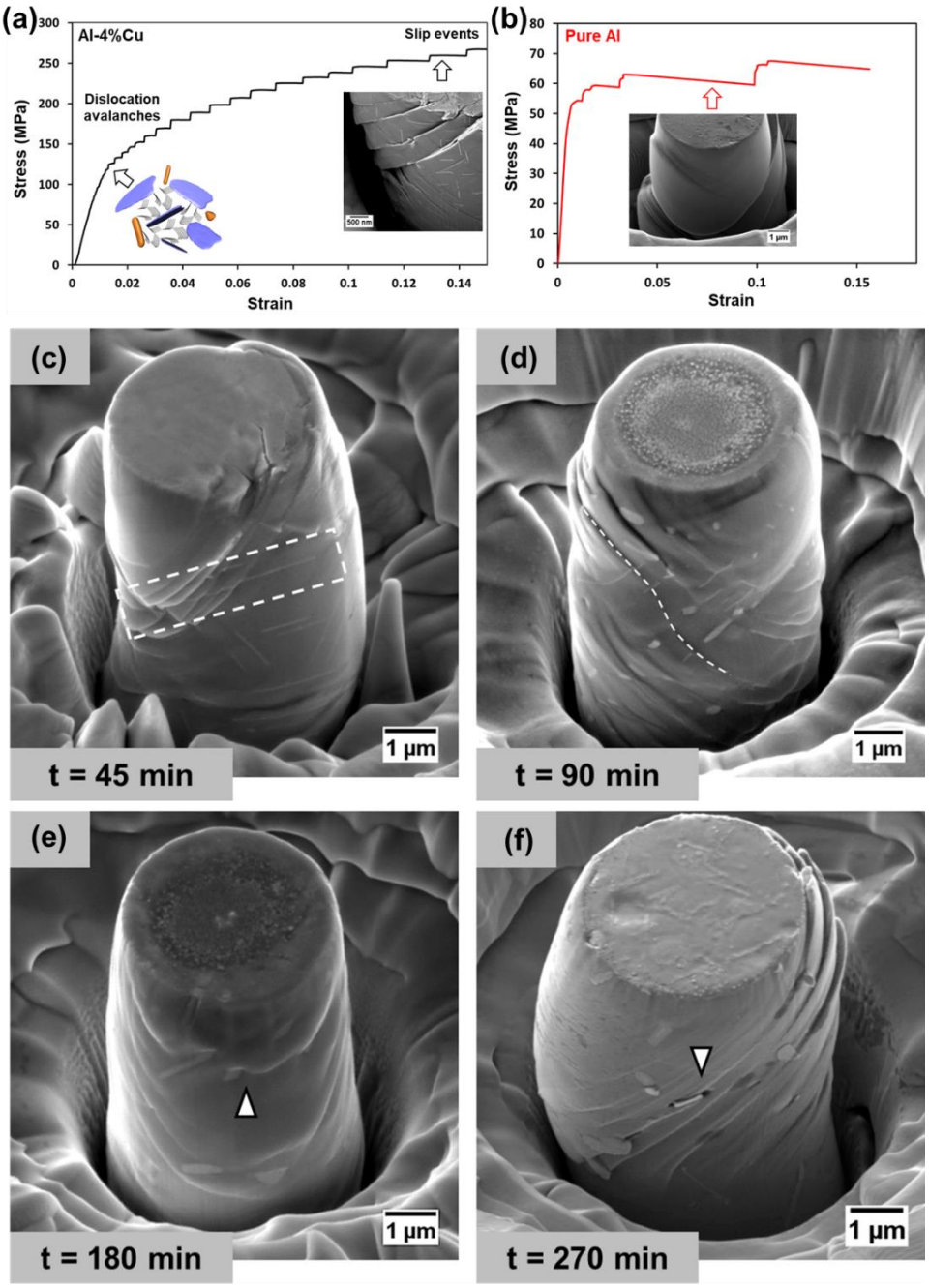

Figure 8: Engineering stress-strain curves obtained from uniaxial compression of micropillars on an (a) Al-4%Cu alloy (aged to t= 45 mins) and (b) Pure Al. Post-compression SEM micrographs of representative micropillars at aging times (c) t= 45 min, (d) t= 90 min, (e) t= 180 min and (f) t= 270 min.

This transition in deformation behavior has also been clearly captured using *in situ* micropillar compression. For the *in situ* tests, micropillars were fabricated at the sample's edge (with

perpendicular faces polished) (Figure 9(a)) on separate samples for the initial (t= 45 mins) and final (t= 270 mins) aging conditions, to allow clear viewing of the indentation process. At the initial aging condition, Figure 9(c) shows the sudden initiation and propagation of slip bands through the micropillar, shearing a couple of θ′ precipitates on its path, as visible from the micropillar's surface. This suggests that once the internal stresses are high enough, the onset of failure can be instantaneous, causing slip to propagate even through thick θ′ precipitates (thickness >60nm). Whereas for the overaged condition, Figure 9(d) shows much smoother deformation in the micropillar. The primary slip bands can be seen avoiding interaction with the shear-resistant θ precipitates, while a few are also impeded at the interfaces of such particles (indicated in Figure 9(d)), leading to interfacial de-bonding. The overall reduction in strain hardening (as a result of aging) has also been clearly captured in the stress-strain curves shown in Figure 9(b) (recorded during in *in situ* micropillar compression testing). A reduction in isotropic hardening is expected as a result of the decrease in the ability of precipitates to store dislocations, due to the decreasing volume fraction of θ′. We can also expect a decrease in kinematic hardening due to a change in the overall morphology of the precipitates.

It is also very interesting to note that although the θ′ precipitates are significantly thick (>60 nm), they are seen to be sheared during micropillar compression. This is quite unconventional as the θ′ phase (Al_2Cu) is considered to be highly shear-resistant, with very high theoretical shear strength values, on the order of GPa [30]. This also suggests that locally very stresses can be attained in such microstructures. Another interesting point to note is that it could be potentially possible that the thickness of a θ′ precipitate determines its ability to store a large density of dislocations, irrespective of its size.

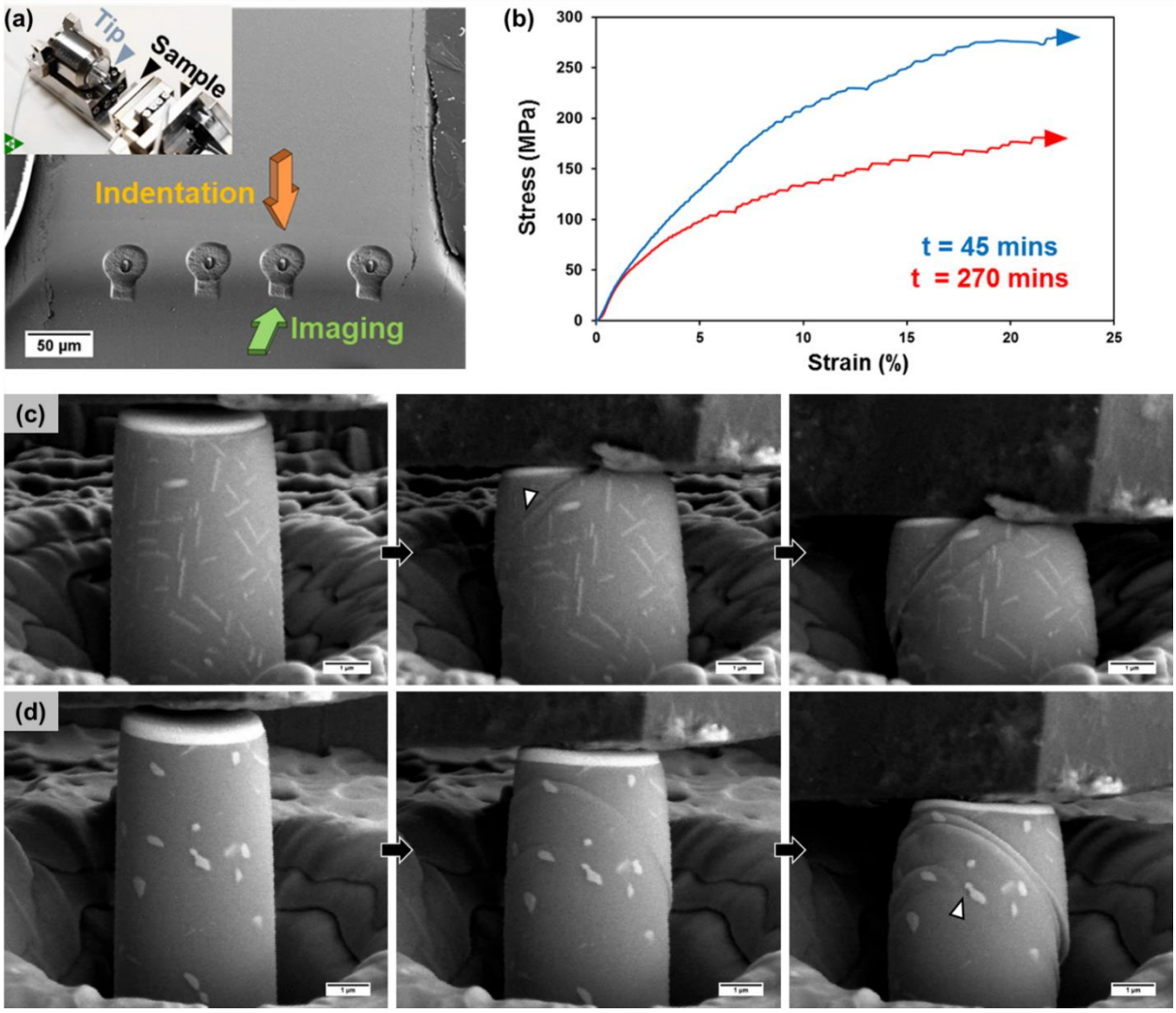

Figure 9: (a) SEM Image showing micropillars fabricated at the edge of a sample. Inset showing the *in situ* indenter NanoFlip's setup. (b) Representative engineering stress-strain curves recorded during *in situ* micropillar compression testing. Stills from video showing *in situ* uniaxial compression of a micropillar aged to (c) t= 45 min and (d) t= 270 min.

Modeling the Variation in Yield Strength using 3D TXM data

Although deformation behavior of Al-Cu alloys has been investigated in detail by several authors in the recent past [28]–[31], a fundamental understanding of the precise deformation mechanisms taking place is still missing. This is mainly because conventional modes of characterizing nanoscale features have been either through transmission electron microscopy [32], which offers

only a sectional view of the specimen, or more recently, atom probe tomography [33], which is capable of sampling statistically insufficient volumes. The main drawback of the aforementioned techniques, however, is their destructive nature. It has been really difficult, to-date, to probe evolution of the same microstructure at the nanoscale, non-destructively over time. This opens up the possibility of drawing conclusions from the mechanical properties of miniaturized volumes from a single grain, to a non-destructively characterized 4D microstructure (a 3D microstructure varying with time).

It is important to note that volume fraction changes occurring in the evolving microstructure can strongly affect the morphological distribution of precipitates in the microstructure. As the θ′ phase is primarily plate-shaped and exists as three orthogonal variants, it is capable of dislocation storage to a much greater extent than the θ phase, which is either globular or rod-shaped. As aging progresses, θ′ plates dissolve and the θ phase nucleates and grows, as a result of which, the alloy's yield strength as well as its strain hardenability reduces. Several authors have previously identified the importance of the precipitate distribution's morphology in determining the mechanical properties of aluminum alloys [28], [34]. However, the models proposed to account for the plate-shaped nature of precipitates in aluminum alloys are either based on idealized microstructures or stereological interpretation of TEM images and hence, do not account for the statistical variability associated with 3D distributions. Figure 10(b) shows the 3D rendering of a non-destructively characterized volume from the micropillar shown in Figure 10(a). By determining the crystallographic orientation of the single-crystalline micropillar's Al matrix using EBSD, it was possible to re-section this virtual microstructure along the (111) plane to determine the precipitate distribution on the aforementioned plane using Avizo® Fire. This corresponded to a single crystal as the grain sizes of the sample under study were made intentionally quite large (~400 μm). A representative slice from this re-sliced microstructure has been shown in Figure 10(c). Scripts in commercial MATLAB® software (MathWorks Inc.) were written and executed to compute the minimum planar inter-particle spacing between adjacent precipitates (λ_{2D}), for each slice of the microstructure, by 2D finite body tessellation using Euclidean distance maps. Figure 10(d) shows the histogram of 2D inter-particle spacing between adjacent precipitates (λ_{2D}) for the initial (t= 45 min) and final aging times (t= 270 min). This provides a glimpse into the complexity of the microstructure.

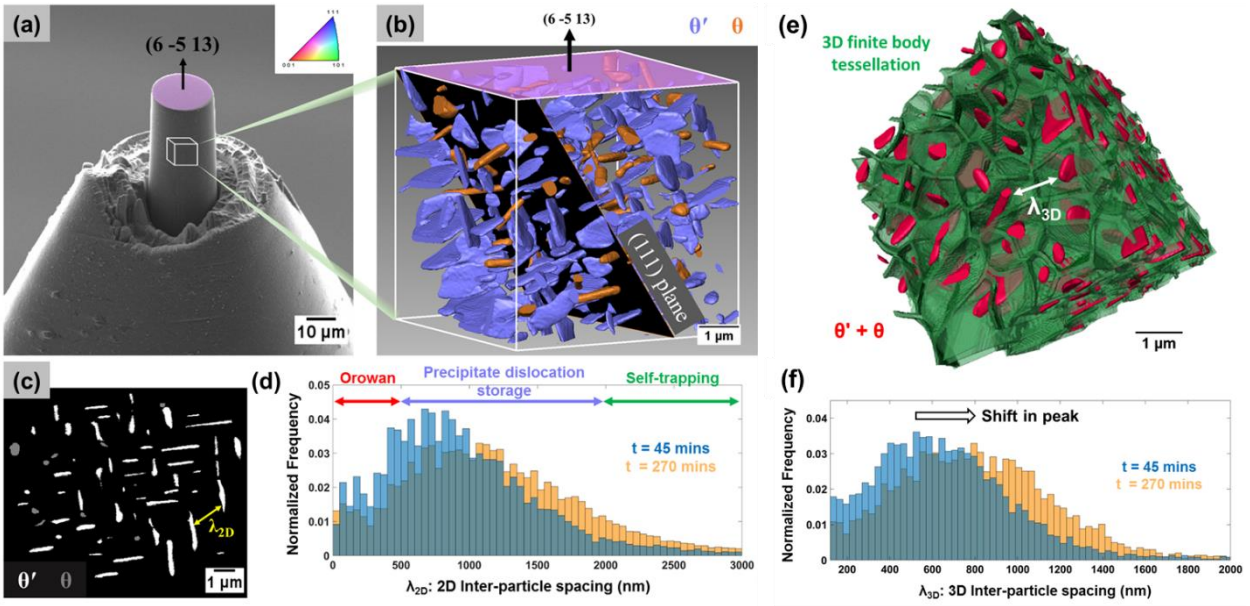

Figure 10: (a) SEM Image of a micropillar fabricated at the tip of an Al-4%Cu alloy needle, for scanning using the Transmission X-ray Microscopy (TXM). Crystallographic orientation of the α-Al matrix at the pillar's top surface measured using EBSD has been shown. Inset shows the IPF map of Al. (b) Non-destructive 3D visualization of a small volume from within the micropillar, showing the different phases (θ′ & θ). (c) Virtual re-slicing of the 3D microstructure showing spatial distribution of precipitates on the (111) plane. (d) Normalized histogram showing distribution of 2D inter-particle spacing between adjacent precipitates on all (111) planes and their classification based on dislocation activity. (e) 3D finite body tessellation using Euclidean distance maps on the 3D microstructure (t= 45 min) to compute the inter-particle spacing between adjacent precipitates. (f) Normalized histogram showing distribution of these 3D inter-particle spacing between adjacent precipitates for the initial and final aging conditions.

The larger size of precipitates present in these aluminum alloys suggest the operation of the following deformation mechanisms: Orowan strengthening, Solid solution strengthening and Dislocation cell strengthening. It's also possible to use the 3D microstructural dataset to quantify the relative proportions of each. In regard to this, several important conclusions can be drawn from this histogram. The Orowan strengthening mechanism is mainly operative only at inter-particle spacings below 500 nm.

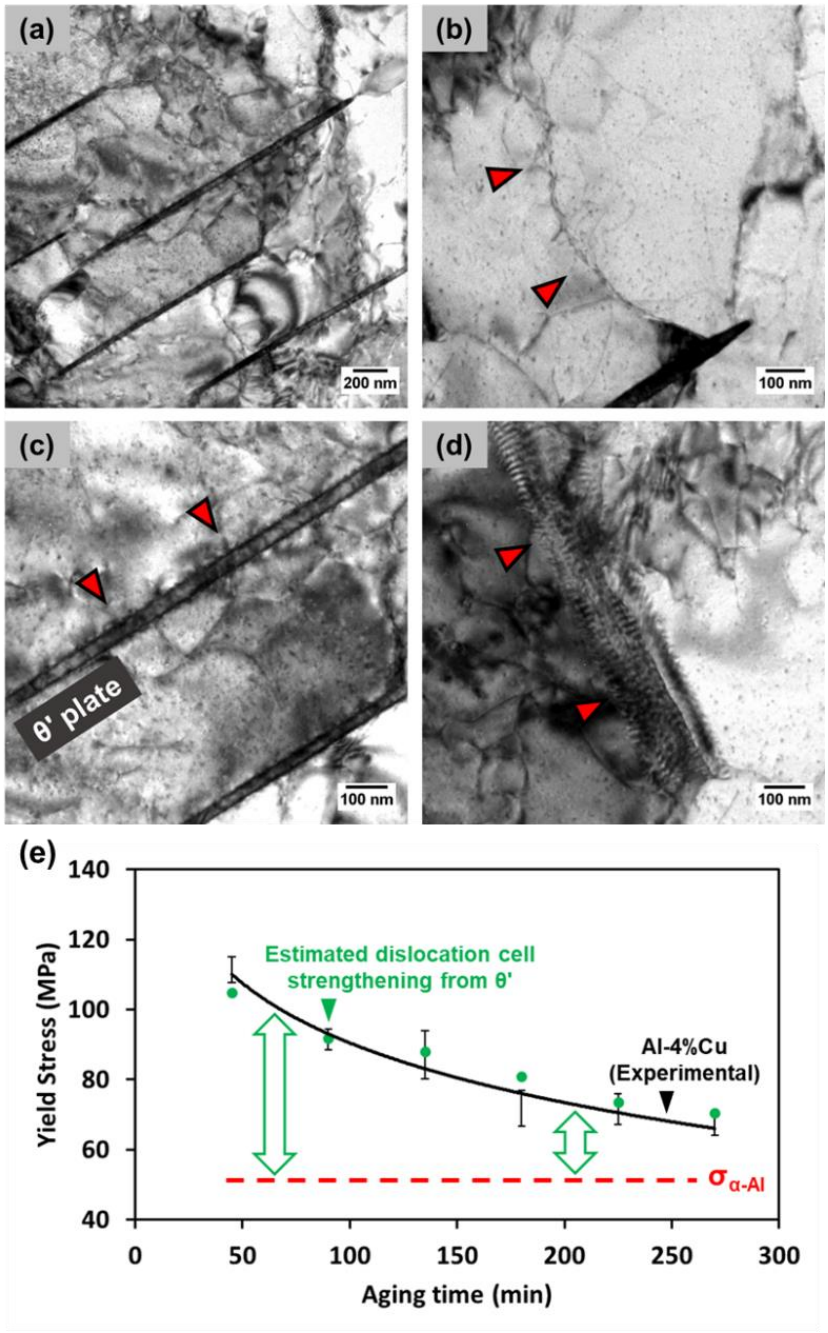

Figure 11: TEM micrographs showing dislocation activity in a representative micropillar at the initial aging condition (t= 45 mins), compressed to its yield point. Formation of dislocation cell structures between precipitates in seen in (a) and (b). Edge-on view of dislocation accumulation on the interfaces of θ′ precipitates is seen in (c). Face-on view of similar dislocation storage on the interface of a θ′ plate is shown in (d). (e) Variation in yield stress estimated with the proposed model using the 3D microstructure compared with experimentally measured values.

TEM observations in Calabrese & Laird's study [29] on the deformation behavior of coarse θ′ plates (similar to those encountered in this study), can be used to support this proposition. Once the inter-particle spacing between precipitates exceeds a certain value (the self-trapping distance), dislocations tend to interact with one another and form dislocation cells, rather than interact with second-phase precipitates. In a fatigue study conducted by Park et al. [35], similar observations were made from precipitates spaced apart greater than 500 nm. However, it must be noted that this transition is not very definite and the assumed value is qualitative. Furthermore, it is also important to note that the contributions arising from Orowan strengthening are quite low at inter-particle spacings greater than 500 nm and hence, do not greatly influence the average computed value. For inter-particle spacings between 500 nm and 2 μm, storage of dislocations at precipitate interfaces plays a dominant role in controlling deformation. Numerous dislocation cells are formed within the matrix and the walls of these cells are defined by the precipitate interfaces. Hence, the precipitates play a pivotal role in determining the dislocation cell size, as also observed in Calabrese & Laird's study [29]. However, at larger inter-particle spacings (> 2 μm), mutual interactions between dislocations tend to supersede all other interactions and the dislocation cell size is no longer a function of the precipitate morphology. In this fashion, the inter-precipitate spacing histogram can thus be classified into three domains.

As the majority of the distribution belongs to the second domain, dislocation storage is directly influenced by the size, distribution and morphology of the precipitates present. It can also be conjectured that the Orowan mechanism operates only later in the deformation process, when the internal back stresses generated from dislocation pile-up on precipitate interfaces rise significantly (after the onset of plasticity). Using parameters acquired by virtually re-slicing the 3D datasets, an upper bound value for the increase in CRSS from Orowan strengthening can be accurately calculated from [26], [27]:

$$\Delta\tau_p = \frac{Gb}{2\pi\lambda_{Mean2D}\sqrt{(1-\nu)}} ln\left(\frac{D_p}{b}\right) \quad (4)$$

where G is the shear modulus of the aluminum matrix, v is Poisson's ratio, λ_{Mean2D} is the average planar inter-particle spacing (<500 nm), D_p is mean planar particle diameter and b is the magnitude of the burgers vector of dislocations in the matrix. As only contributions from the first domain of the histogram are considered, the upper bound value for increment in CRSS from Orowan strengthening does not vary significantly with aging time and is found to be ~20 MPa.

Similarly, it is also possible to quantify the contribution from solid solution strengthening using the Fleischer equation [36]. As the copper dissolved in solution is only 0.6 wt. %, this value is negligible and hence, the effects from solid solution strengthening can be safely ignored. Variation in yield strength is hence primarily dictated by the density of geometrically necessary dislocations (GNDs) and the size dislocation cells formed between precipitates. It is well known that these dislocations can tend to form complex three-dimensional networks intertwined with the precipitates [29], [31]. Hence, understanding the three-dimensional spatial distribution of θ′ and θ precipitates is indispensable in estimating the size of these dislocation cell structures. For this purpose, similar scripts in MATLAB® (MathWorks Inc.) were used to compute the minimum 3D inter-particle spacing between adjacent precipitates (λ_{3D}), by 3D finite body tessellation using Euclidean distance maps, as shown in Figure 10(e). Figure 10(f) shows the histogram of 3D inter-particle spacing between adjacent precipitates (λ_{3D}) for the initial (t= 45 min) and final aging times (t= 270 min). These are evidently quite different from those in Figure 10(d), hence highlighting the need to probe the 3D spatial distribution of precipitates.

Russel and Ashby [31] found large gradients in shear in the vicinity of similar coarse θ′ precipitates by measuring asterism in Laue patterns and using transmission electron microscopy. From their work, it is clear that the local shear strain (γ) at the particle-matrix interface caused by interaction of a slip system from the matrix, is a function of the density of GNDs stored at these interfaces. This leads to local lattice rotation in the matrix. Evidence of dislocation storage, in the current study, on the broad faces of plate-like θ′ precipitates can also be seen from TEM Images shown in Figure 11. This TEM specimen corresponds to a section of a micropillar (initial aging condition, t= 45 min) compressed to its yield point. Strain contrast from accumulation of dislocations at the interface of θ′ (edge-on view) is visible in Figure 11(c). Figure 11(d) shows an array of dislocations stored at a θ′ precipitate (face-on view). The dislocation spacing on θ′ precipitates from these TEM micrographs was used to compute the shear strain ($\gamma \sim 0.012$) using the relation $nb = \gamma h$ [31], where h is the plate height normal to the slip plane. The density of GNDs (ρ^G) trapped by the globular/rod-shaped θ phase can be neglected (for purposes of γ calculation) as it is considerably lower and Ashby's work [37] has been able to quantify this. This can also be concluded qualitatively from Brown and Stobbs' work [38], relating the plastic strain to the number of dislocation loops stored by such particles. Assuming that there exists a minimum spacing between loops [30], the θ phase stores a considerably lower density of GNDs,

as a result of their morphology. Ease of cross-slip in aluminum alloys also reduces the probability of dislocations interacting with elongated θ precipitates. Accounting for these factors, the local shear strain (γ) can also be directly related to the total 3D surface area of θ′ precipitates ($A_{\theta'}$) owing to their ability to store a high density of dislocations: $\gamma \, \alpha \, A_{\theta'}$. As a result of 3D nanoscale characterization, the total 3D surface area of θ′ precipitates ($A_{\theta'}$) can be accurately computed from Avizo®. Quantitative estimation of the shear strain γ (as mentioned above, using TEM micrographs of the sample at t= 45 min) can be coupled with the aforementioned proportionality relationship to compute the shear strain (γ) for the remaining aging conditions. These parameters can then be related to the yield strength (σ_y) using a variant of the relation used in Ref. [31],

$$\sigma_y = \sigma_{\alpha-Al} + \frac{0.35G}{m}\sqrt{b\gamma/\lambda_{Mean3D}} \quad (5)$$

where γ is the local shear strain, b is the magnitude of the burgers vector of dislocations in the matrix, λ_{Mean3D} is the mean three-dimensional inter-particle spacing of the precipitate ensemble, G is the shear modulus of the Al matrix, m is the corresponding Schmid factor. As the crystallographic orientation of the Al matrix was pre-determined using EBSD, Schmid factor analysis was used to compute m (=0.41) and determine the active slip system: $(1\bar{1}1)$ $[\bar{1}01]$. Although previous studies have roughly approximated "λ_{Mean3D}" using stereological deductions, its accurate value can only be estimated using three-dimensional characterization of the bulk microstructure, as in the current case. $\sigma_{\alpha\text{-Al}}$ represents the base strength of the Al matrix caused by statistically stored dislocations (shown in red, Figure 11(e)). This was measured by testing pure Al micropillars of similar size, to avoid inclusion of any effects arising from image stresses or size of the micropillars. The yield strength (σ_y) estimated from the above model (shown in green, Figure 11(e)) was seen to be in excellent agreement with the values measured experimentally using micropillar compression (shown in black, Figure 11(e)). The minor deviations from the trend that are seen can be attributed to the stochastic nature of plasticity onset in micropillars, which can affect the precise determination of yield stresses during uniaxial compression of such micrometer-sized volumes of material.

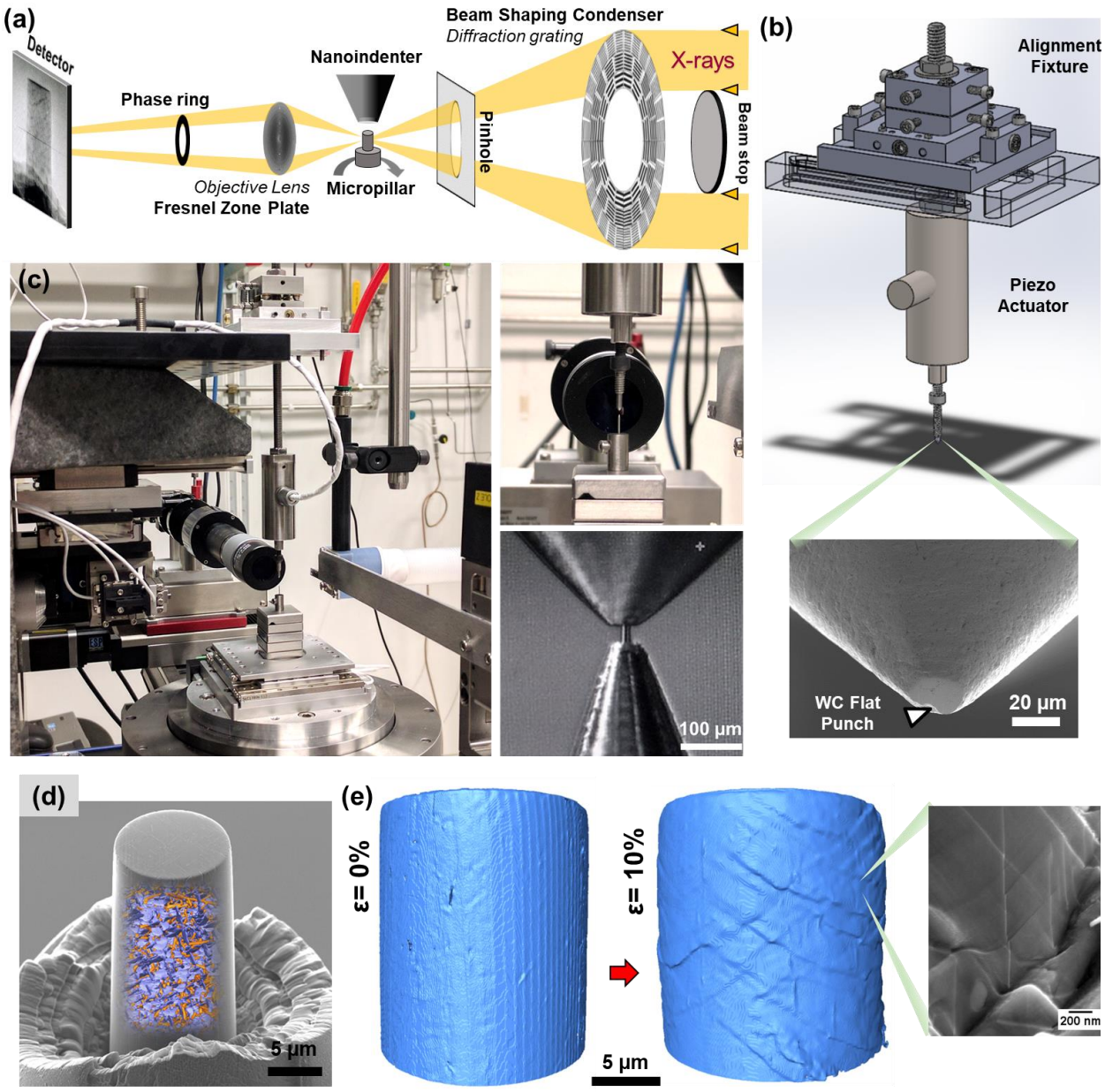

Figure 12: (a) Schematic of TXM setup along with the *in situ* Nanoindenter, shown in (b) and (c). (d) SEM micrograph of micropillar fabricated at needle tip for *in situ* testing. (e) 3D rendition of the micropillar with strain showing formation of shear bands on its surface.

In situ 4D Nanomechanical testing

Although *in situ* studies performed in the SEM can be insightful, monitoring nanoscale structural changes in 3D non-destructively to understand the alloy's deformation behavior can have colossal implications in refining alloy design approaches. A state of the art compact nanoindentation system was designed to carry out micro-compression and capture the initiation and evolution of damage at the nanoscale in 3D. 3D tomographic imaging at such high spatial resolutions (sub-60 nm) requires design of a specialized stable sample stack devoid of any mechanical vibrations or thermal drift. The sophisticated stage design at sector 32-ID-C [39] allows imaging without the use of any digital drift correction procedures which are conventionally used for aligning the 3D stack. To render mechanical testing of such miniaturized volumes possible without compromising the quality of 3D imaging, it was also necessary to custom design the system to be suspended mid-air atop the sample. This system was hooked onto a large granite wedge that serves to hold the zone plate objective lens assembly in place.

The alignment fixture (Figure 12) aided in precise axial and angular positioning of the tungsten carbide (WC) flat punch over the micropillar top. 2D projections from the TXM were used in conjunction with a perpendicularly placed optical microscope to aid in precise positioning. As the micropillar was compressed, 3D nanoscale imaging at incremental strains was performed to probe the evolution of damage in the precipitation-strengthened Al-Cu alloy. Onset of plasticity in such materials is marked by shear bands propagating along slip planes with highest CRSS values. FCC nature of aluminum results in more than one such slip system operating due to their comparable CRSS values, which can be clearly seen in the 3D rendition of the micropillar's surface relief shown in Figure 12 and 13. Micropillar compression serves as an ideal technique to monitor the deformation response of a material at the micro and nano length scales. However, so far understanding their micro-mechanical response has mostly been limited to surface analyses only using SEM. It is important to note that this can be quite misleading owing to the difference in stress states in the interior and at the surface of the micropillar. Ordered $CuAl_2$ precipitates have been commonly reported as brittle intermetallic particles that strengthen the Al matrix and eventually get sheared at large strains. SEM observation of the surface also suggests the same (Figure 12(e)). However, further inspection in the bulk of the micropillar using 3D non-destructive nanoscale imaging reveals buckling and kinking of thicker θ' precipitates dispersed in the path of these shear bands, revealing their ability to plastically

deform to an unprecedented extent. Figure 13(d) shows the evolution of this deformation kink in precipitates as a function of strain. Evidence of a substructure was also found from SEM micrographs (Figure 13(c)). FIB cross-section on the deformed pillar, followed by EBSD revealed that the kinked precipitates are mostly present along shear bands, associated with high degrees of misorientation.

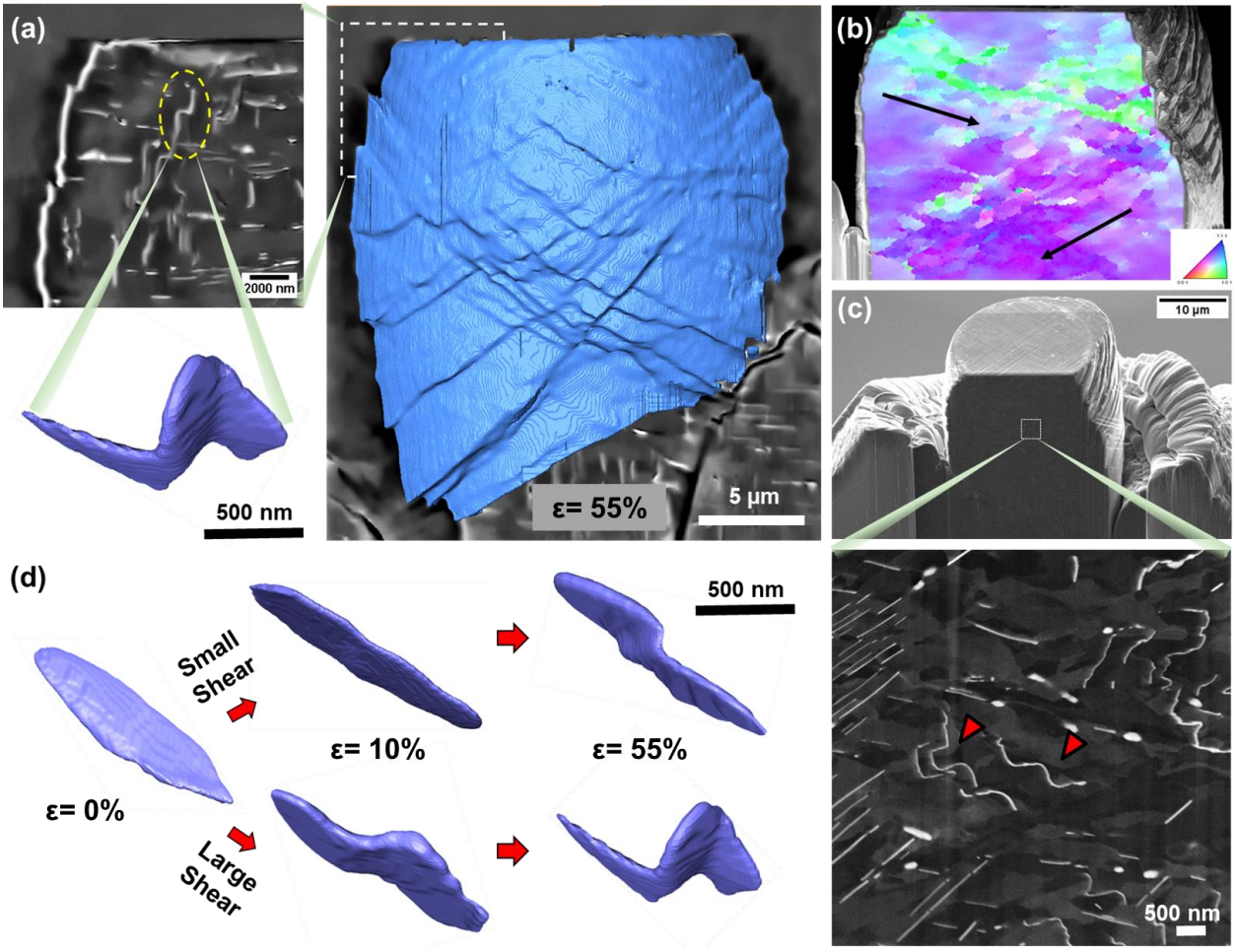

Figure 13: (a) 3D rendition of deformed micropillar showing intersecting slip bands on its surface. (b) EBSD on the FIB cross-sectioned face of the micropillar. (c) SEM micrographs revealing the presence of a substructure in the matrix. (d) 3D rendition of deformation kink evolution in precipitates as a function of strain.

Experimental conclusions

Precipitate strengthened materials achieve improved mechanical strength by effectively impeding the dislocation motion. These material microstructures are generally prepared based on the idea that the increase in precipitate size causes a transition in the mechanism that the dislocation uses to overcome the precipitate thereby requiring larger shear stress. In other words, during the aging process the precipitate changes from being easily sheared to impenetrable to dislocations as precipitate size increases. However, in this work we have shown that the orientation and planar density of the precipitate at the dislocation glide also can alter the mechanism and the critical shear stress. This motivated us to quantify the critical shear stress for several scenarios of dislocation-θ' Al_2Cu-precipitate interaction for both edge and screw character. Finally, this is the first time several precipitate dislocation interaction scenarios have been quantified using a consistent framework at the atomistic length scale. These findings can provide essential information to accurately study precipitate hardened materials at the continuum length scale.

On the Experimental front in the present study, synchrotron-based X-ray Nano-CT has been utilized to address some of the most fundamental metallurgical questions pertaining to precipitation-strengthened systems. The morphology, distribution as well as the evolution behavior of θ′ and θ precipitates in an Al-Cu alloy were studied. Aging at 350 ^{o}C revealed complex transformation reactions that were occurring in the alloy, most of which are nearly impossible to capture using other characterization techniques. 3D measurements of precipitate dimensions rendered a more thorough understanding of the coarsening behavior of θ at 400 ^{o}C. A transition from interface-controlled to volume diffusion controlled growth in thickness was captured from the scaled PSD curves. Correlation of 3D tomography data with EBSD has allowed experimental estimation of the Orowan strengthening as well as quantification of the preferred orientation of the θ phase in 3D. a comprehensive analysis of the deformation behavior in an Al-Cu alloy using a combination of 3D Microstructural characterization (using TXM) and micro-scale mechanical testing, with the aid of TEM and EBSD, has been presented. Three-dimensional morphological parameters and TEM Images were used to accurately model the variation in yield stress as a function of aging time. It was also possible to quantify contributions from the Orowan and solid-solution strengthening processes, using the 3D microstructure.

Histograms of 2D and 3D inter-particle spacings provided novel insights into understanding the deformation mechanisms in such alloys. *In situ* uniaxial micro-compression experiments allowed vivid visualization of the deformation processes. The strain bursts observed in stress-strain curves were directly correlated to live shearing events in the SEM. Whereas, 4D Nanomechanical testing allowed us to capture initiation and propagation of damage in micropillars in 3D as a function of strain.

Multiscale modeling

Crystal plasticity simulations

In order to engineer the microstructure of precipitate-hardened alloys, mechanical testing under controlled conditions is required to parametrically study the effect of different factors. Although valid experimental findings are usually the most reliable resources, carrying out such procedures can be quite time-consuming and expensive. Meso-scale crystal plasticity simulations, on the other hand, can be quite helpful in reducing the number of necessary experiments in a study and can provide us with certain data that are impossible or tedious to capture through regular experimental procedures [40]. To get reliable results, however, meso-scale simulations have to accurately take into account the alloy composition (microstructure), texture, etc. Only then a multi-scale continuum analysis can help us better understand deformation mechanism. In order to build up a robust crystal plasticity framework, first microstructural information from experimental study should be transferred into the modelling domain to accurately represent the alloy. These experimental data are either directly used in the simulations in terms of representative volume elements (RVEs), or indirectly provide information necessary to evaluate the material model such as critical resolved shear stress [40].

Usually, experimental statistical quantities are required to reconstruct the microstructure for meso-scale simulations. But here, the studied alloy Al-4wt.%Cu is known to have a rather ordered microstructure, as showed before. Hence, we use high-resolution 3D reconstructed experimental images obtained in the first sections at different aging times to directly import the microstructure into the simulation tool in such a way that it represents the whole micro-pillar.
The primary goal here is to present a crystal plasticity model that is able to reproduce the experimental yield measurements of micro-pillars at different aging times. Then the model is used for a parametric study on the matrix-precipitate interactions.

Model and simulation details

In this section the crystal plasticity model and simulation procedure are described. DAMASK crystal plasticity material simulation kit with spectral solver was used for all the continuum scale

simulations [41]. In the conventional FEM tools, the imported reconstructed microstructure is meshed using complex meshing algorithms. But here, the images are directly used in DAMASK. In other word, each image voxel represents an integration point in the simulation domain, which eliminates the laborious step of meshing. Moreover, the spectral method used in DAMASK has been proven to be much more efficient compared to the conventional finite element method (FEM) both in terms of spacial resolution and convergence speed [40], [41].

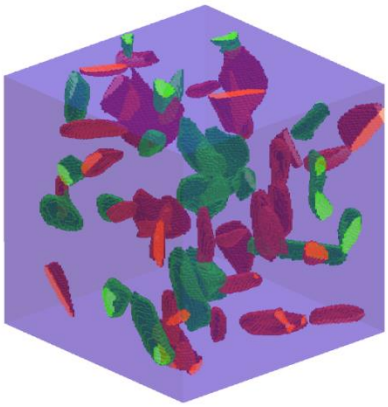

Figure 14: Three phases in an RVE: Aluminum matrix (purple), θ precipitate (green) and θ' precipitate (red).

Appropriate deformation gradient and complementary stress tensors were used in the solver to mimic a compressive loading condition in the studied cases here [41]. Convergence was guaranteed by using a grid of 128x128x128 for each case study. Each RVE has three distinct phases: The Al matrix, θ and θ' precipitates (see Figure 14).

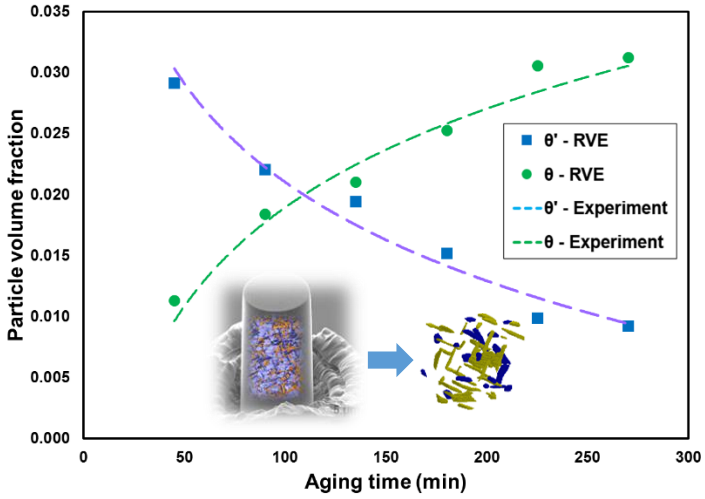

Figure 15: θ and θ’ precipitates volume fractions for different aging times measured from the expeimental data (dashed lines) and used in simulations as RVEs (solid markers).

Experimental 3D images (converted to voxel data) were cropped to a sufficiently large cube and used as the simulation grid points. This was carried out is such a manner that the cropped cubes had almost the same particle volume fractions as the micro-pillars. Figure 15 shows θ and θ’ precipitates volume fractions for different aging times measured from the expeimental data and the simulated RVEs.

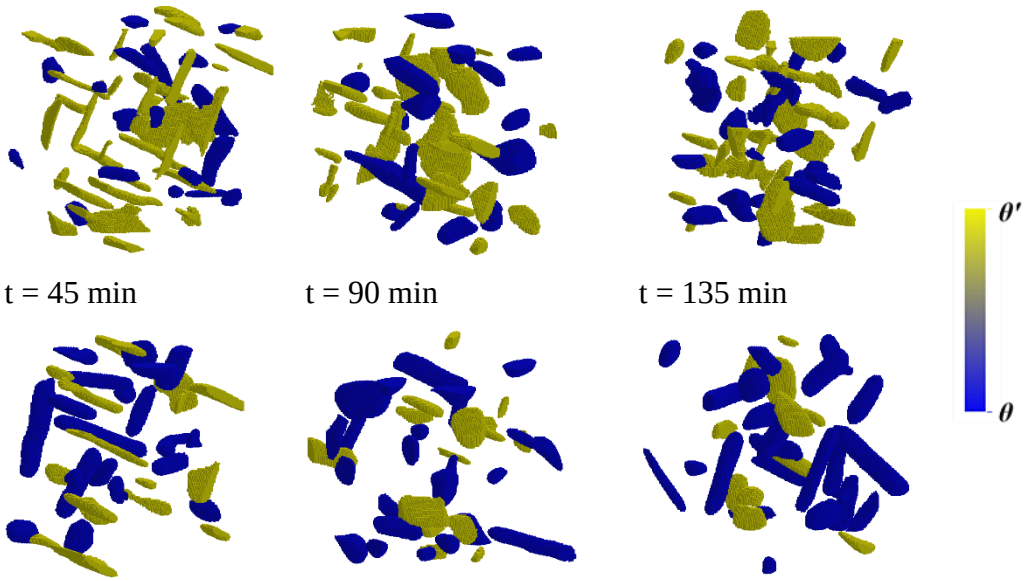

t = 180 min t = 225 min t = 270 min

Figure 16: θ (blue) and θ’ (yellow) precipitates in RVEs for different aging times (t) used in simulations (Al matrix is not shown here for clarity).

Individual θ and θ’ in the simulated RVEs at different agint times are depicted in Figure 16. In the next section, the phenomenological crystal plasticity constitutive law is presented.

Kinematics and constitutive equations

A simple and well-known phenomenological crystal plasticity constitutive equations is used in this study [42]. The total imposed deformation gradient is multiplicatively decomposed as follows:

$$\mathbf{F} = \mathbf{F}^{*}\mathbf{F}^{p} \quad (6)$$

where $\mathbf{F}^{*}$ and $\mathbf{F}^{p}$ represent elastic (stretch and rotation) and plastic parts of the total deformation gradient. The schematic of the decomposition is shown in Figure 17.

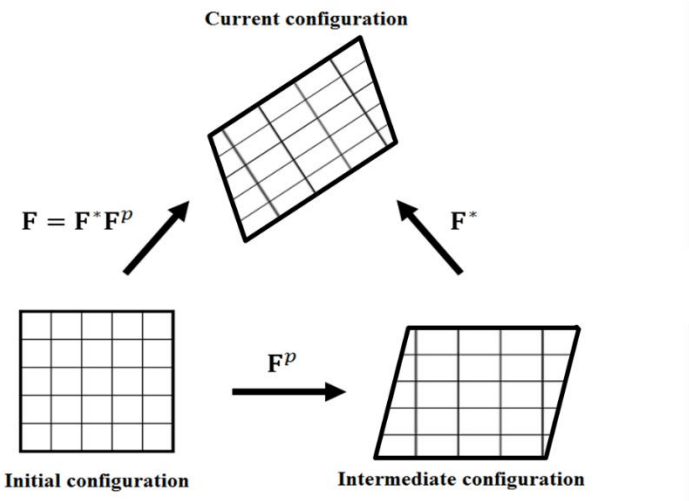

Figure 17: Multiplicative decomposition of the deformation gradient tensor [43].

For the elastic response, a constitutive equation for a single crystal that related the second Piola-Kirchhoff stress tensor $\mathbf{T}^{*}$ to its energy conjugate Green-Lagrange strain tensor $\mathbf{E}^{*}$ is expressed

as $\mathbf{T}^* = \mathbf{C}\mathbf{E}^*$where $\mathbf{C}$ is the fourth order anisotropic elasticity tensor. $\mathbf{T}^*$ and $\mathbf{E}^*$ are defined as [44]:

$$\mathbf{T}^* = J\mathbf{F}^{*-1}\mathbf{T}\mathbf{F}^{*-T} \tag{7}$$

$$\mathbf{E}^* = \frac{1}{2}\{\mathbf{F}^{*T}\mathbf{F}^* - \mathbf{I}\} \tag{8}$$

where $\mathbf{T}$ is the Cauchy stress and the Jacobian J is the determinant of $\mathbf{F}^*(J > 0)$. Time derivative of the plastic part of the deformation can be related to its velocity gradient by [44]:

$$\dot{\mathbf{F}}^p = \mathbf{L}^p\mathbf{F}^p \tag{9}$$

where

$$\mathbf{L}^p = \sum_{\alpha}^{N^{\text{slip}}} \dot{\gamma}^{\alpha}\mathbf{S}_0^{\alpha} \tag{10}$$

$\mathbf{S}_0$ in the above equation is the Schmid tensor ($\mathbf{m}\otimes\mathbf{n}$) for slips defined using the initial crystallographic orientation. N^{slip} is the total number of slip systems. $\dot{\gamma}^{\alpha}$ is the slip rate on the α th slip system ($\alpha = 1,2,\dots,12$). The slip rate on slip system α is governed by Asaro and Needleman power-law equation [42]:

$$\dot{\gamma}^{\alpha} = \dot{\gamma}_0 \left|\frac{\tau^{\alpha}}{S^{\alpha}}\right|^{\frac{1}{m}} \text{sign}(\tau^{\alpha}) \tag{11}$$

τ and S in Eqs. (10) and (11) are the resolved shear stress ($\tau = \mathbf{T}^*.\mathbf{S}_0$) and resistance, respectively, for slip (α) systems. In the above equations, m is the rate sensitivity parameter. More detailed description of the kinematics and the constitutive equations can be found in [45] and [44]. Moreover, the evolution of slip hardenings is described by the following phenomenological relation [44], [45]:

$$\dot{S}^{\alpha} = h_0(1 - s^{\alpha}/s_s^{\alpha})^w h_{\alpha\beta}\dot{\gamma}^{\beta} \tag{12}$$

In the above equations, the material parameters h_0 represent hardening rates (modulus) associated with the slip and the coefficient matrix $h_{\alpha\beta}$ determines the interaction of coplanar and non-coplanar slips ($\beta = 1,2,\ldots,12$). S_s^{α} is the overall saturation value of the slip system α. In Eq. (12), w is a phenomenological constant that capture the interactions of the slips and deformation twins [44], [46].

Material properties and results

In this section, material properties used in the simulations for the Al matrix, θ and θ' precipitates are provided. Elastic constants for Al matrix (FCC) are taken from the literature [41]. For the precipitates, the elastic constants obtained using DFT calculation were used [47], [48]. It was assumed that for the θ particles, which have a BCT-type crystal structure, only slip with direction of <001> on (110) and (010) planes are active [48]. Elastic constants for the three phases are listed in Table 1. All the plasticity related parameters provided in Table 1 are assigned to the entire domain of simulation. Experimental EBSD orientation measurements of the tested pillars were assigned to the simulation domains as the initial state. The three assigned Euler angles were φ_1=232˚, Φ=32 ˚, φ_2=131 ˚.

Table 1: Values of the parameters used in crystal plasticity simulations

(a) Elasticity						
Al matrix (GPa)	C_{11}=106.7		C_{12}=60.4		C_{44}=28.3	
θ (GPa) [49]	C_{11}=150.3	C_{33}=171.1	C_{12}=86.1	C_{13}=62.6	C_{44}=29.4	C_{66}=45.5
θ’ (GPa)*	C_{11}=192.5		C_{12}=110.5		C_{44}=46.2	
(b) Plasticity						
Property			**Value**			
$\dot{\gamma}_0$ (m/s)			0.001			
h_0 (MPa)			75			
w			2.25			
m			0.05			
Coplanar $h_{\alpha\beta}$			1			
Non-coplanar $h_{\alpha\beta}$			1.4			

*Elastic constants obtained using MD simulations.

To approximate CRSS (τ_0) for each aging time, Schmid analysis was carried out on the micropillar samples. Maximum Schmid factor was determined to be 0.41, which yielded the CRSS values listed in Table 2.

Table 2: CRSS values obtained by Schmid analysis of micro-pillars.

Aging time (min)	**45**	**90**	**135**	**180**	**225**	**270**
τ_0 **(MPa)**	49.2	37.6	33.5	30.8	28.9	27.5

The same CRSS values were assinged to Al matrix in crystal plasticity simulations. For θ and θ' precipitates, shear strengths of 70MPa and 150MPa were assigned based on our previous MD findings. Figure 18 shows the variation of 1% flow stress at different aging times. Red vertical lines in Figure 18 indicate the range of experimental measurements accompanied with a black trend line. The 1% flow stresses obtained from simulations are shown by blue circles. As it can be seen, the crystal plasticity framework can very well reproduce the experimental measurements.

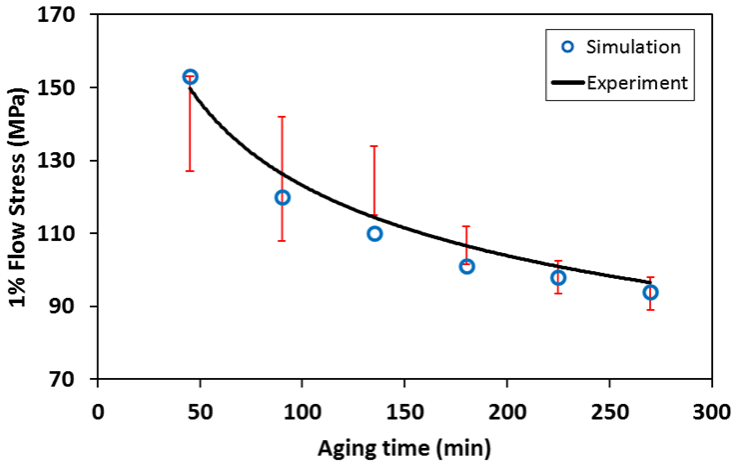

Figure 18: Variation of 1% flow stress at different aging times. Red vertical lines indicate range of experimental measurements with a black trend line.

Figure 19 depicts the contours of plastic slips in a slice of a simulated RVE (t=45min). As indicated by the white arrows, some particles (mostly θ') experience shearing after 10%

compression. Although the micron-scale particles usually have high shear resitance, dislocation pileups can eventually cause either particle shear at favorable sites or particle kinking depnding on the size and orientation properties.

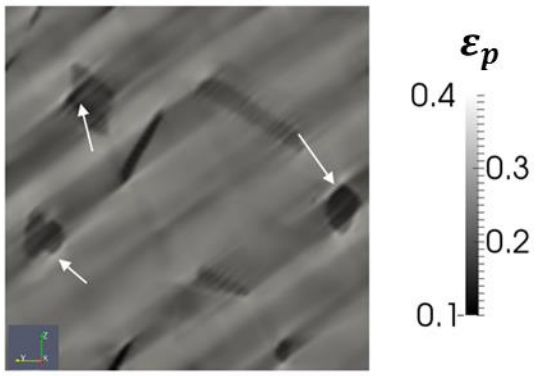

Figure 19: Total shear after 10% compressive strain: Arrows indicate sheared particles.

The particle kinking mechanism was discussed in the experimental section. Here, in order to gain more udnerstanding of the possible matrix-particle interactions leading to θ' particle kinking, a synthetic microstructure with three plate-like particles on planes of type {100} in the Al matrix was simulated under 25% compression along the *z*-axis (see Figure 20). The initial assigned Euler angles were φ_1=0, Φ=0 and φ_2=0 in the Al matrix.

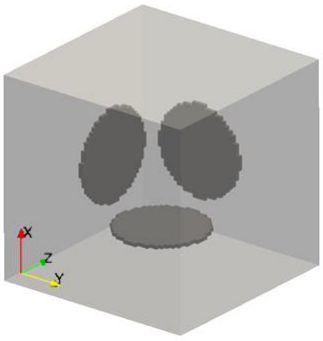

Figure 20: Synthetic microstructure with three *θ'* particles.

The same material properties used for the actual microstructures simulated before were used in this simulation. In Figure 21 (a), the contours of the plastic strain are depicted on a 2D slice in *yz*-plane cutting the simulation domain in half. Interestingly, it was observed that the kinking

deformation of the particles is primarily due to the significant activity of the slips on one or two planes with the highest local resolved shear stresses in the Al matrix. As seen in Figure 21(a), the particle oriented along z-direction experiences significant plastic deformation. Subsequently, this leads to shear localization in the particles and eventually kinking. This proposition has been schematically depicted in Figure 21 (b), where dislocation pileups at certain regions can cause the particle segments to reorient themselves.

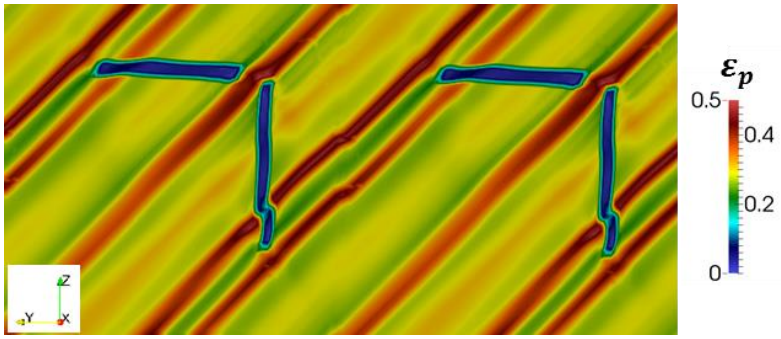

(a)

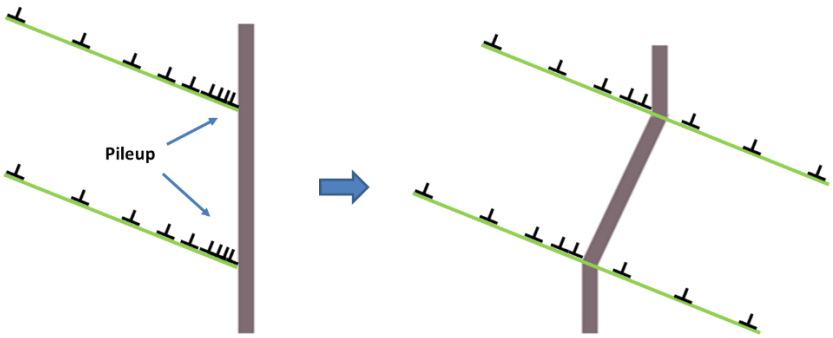

(b)

Figure 21: (a) Contours of plastic strain (shear bands) and particle kinking (note that the domain has been replicated for better visualization of the shear bands), (b) Proposed mechanism for particle kinking due to dislocation pileup.

To further investigate the kinking mechanism, a single θ' particle along <001> was compressed up to 15% total strain along the *z*-direction (see Figure 22). The initial assigned Euler angles were equal to that of an actual tested micro-pillar (φ_1=232˚, Φ=32˚ and φ_2=131˚).

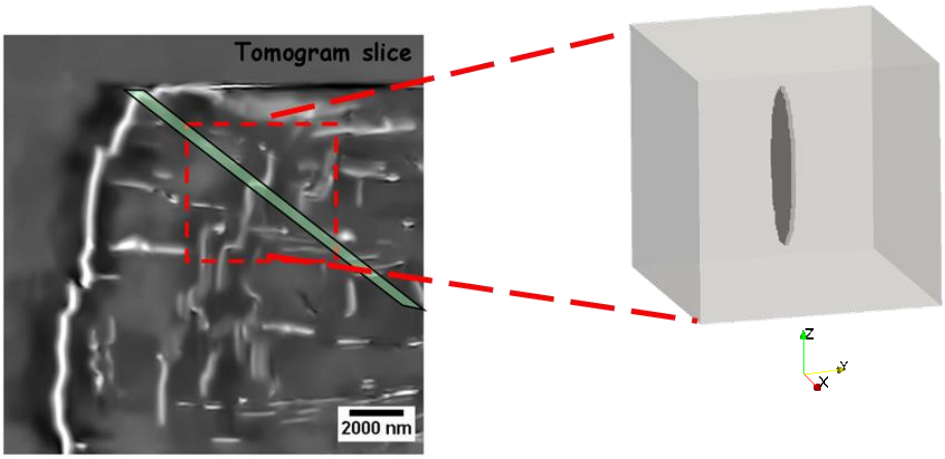

Figure 22: A tomogram slice of a micro-pillar after 50% compression (left) and a synthetic *θ'* single particle in the Al matrix (right).

The aim here was to estimate the average misorientation angle between the undeformed sample and the regions of high slip activity (shear bands) in the vicinity of the particle. Figure 23 (a) shows the total plastic strain in the kinked particle. As it is evident, the particle kinks at regions with the highest slip activity.

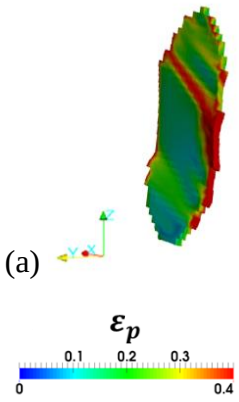

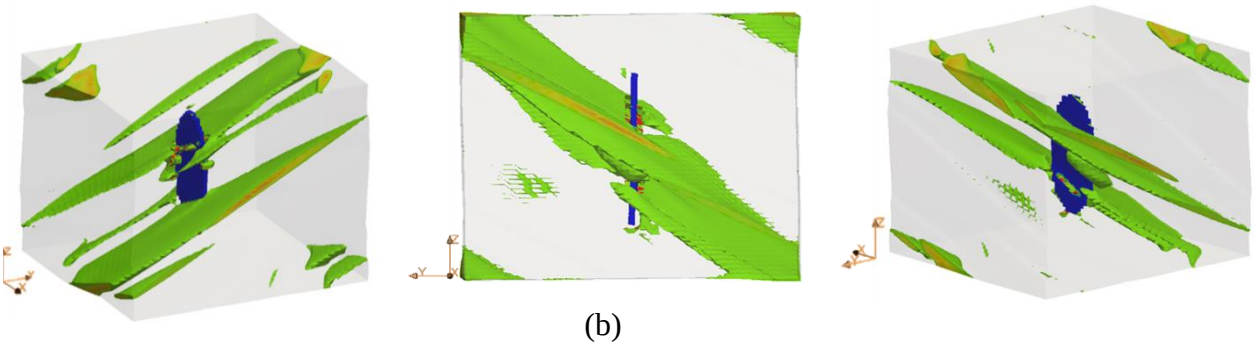

(b)

Figure 23: (a) Plastic strain in the kinked *θ'* particle, (b) Iso-volume shear bands at total 15% compressive strain.

Figure 23 (b) depicts the shear bands due to slip activity impeded by the particle. It is noteworthy that the particle size and spacing can affect the shear band spacing.

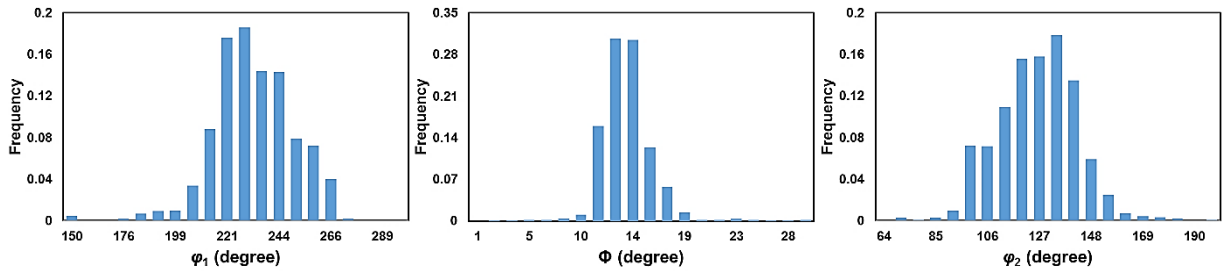

Figure 24: Distribution of the Euler angles in the shear bands after 15% compression.

After 15% defomrmation the distribution of the Euler angle in the shear bands (regions with the highest slip activity) were extracted (see Figure 24). The Euler angle mean values were approximately calculated to be φ_1=229˚, Φ=13˚ and φ_2=134˚. This renders a misorientation angle of about 19.03˚ compared to the less deformed regions.

Multiscale modeling conclusions

A crystal plasticity framework was presented for meso-scale simulations of precipitate strengthened materials with relevant DFT information. Spectral solver along with experimentally captured voxel data of the studied Al-Cu alloy was used to calibrate the model. It was shown that the framework can very well capture the experimentally measured 1% flow stress. In addition, the particle kinking mechanism reported in the experimental section of this study was further

examined using the crystal plasticity simulations of synthetic microstructures. The results showed that the observed kinking is due local severe slip activity on one or two slip planes in the vicinity of the particles and that the orientation of the particle with respect to the active slip is crucial to the probability of kinking.

References

[1] J. D. Boyd and R. B. Nicholson, "The coarsening behaviour of θ″ and θ′ precipitates in two Al-Cu alloys," *Acta Metallurgica*, vol. 19, no. 12, pp. 1379–1391, Dec. 1971.

[2] E. Orowan, "Symposium on Internal Stresses in Metals and Alloys," *Institute of Metals, London*, vol. 451, 1948.

[3] D. A. Terentyev, G. Bonny, and L. Malerba, "Strengthening due to coherent Cr precipitates in Fe–Cr alloys: Atomistic simulations and theoretical models," *Acta Materialia*, vol. 56, no. 13, pp. 3229–3235, Aug. 2008.

[4] Y. N. Osetsky and D. J. Bacon, "Void and precipitate strengthening in α-iron: what can we learn from atomic-level modelling?," *Journal of Nuclear Materials*, vol. 323, no. 2–3, pp. 268–280, Dec. 2003.

[5] Z. Chen, N. Kioussis, and N. Ghoniem, "Influence of nanoscale Cu precipitates in α-Fe on dislocation core structure and strengthening," *Physical Review B*, vol. 80, no. 18, p. 184104, Nov. 2009.

[6] C. V. Singh, A. J. Mateos, and D. H. Warner, "Atomistic simulations of dislocation–precipitate interactions emphasize importance of cross-slip," *Scripta Materialia*, vol. 64, no. 5, pp. 398–401, Mar. 2011.

[7] G. Monnet and B. Devincre, "Solute friction and forest interaction," *Philosophical Magazine*, vol. 86, no. 11, pp. 1555–1565, 2006.

[8] Y. Xiang and D. J. Srolovitz, "Dislocation climb effects on particle bypass mechanisms," *Philosophical Magazine*, vol. 86, no. 25–26, pp. 3937–3957, 2006.

[9] S. S. Chakravarthy and W. A. Curtin, "Effect of source and obstacle strengths on yield stress: A discrete dislocation study," *Journal of the Mechanics and Physics of Solids*, vol. 58, no. 5, pp. 625–635, May 2010.

[10] K. N. Grew *et al.*, "Nondestructive Nanoscale 3D Elemental Mapping and Analysis of a Solid Oxide Fuel Cell Anode," *Journal of The Electrochemical Society*, vol. 157, p. B783, 2010.

[11] C. Laird and H. . Aaronson, "Mechanisms of formation of [theta] and dissolution of [theta]' precipitates in an Al-4% Cu alloy," *Acta Metallurgica*, vol. 14, no. 2, pp. 171–185, 1966.

[12] C. Zener, "Kinetics of the decomposition of austenite," *Trans. Aime*, vol. 167, no. 550, p. e591, 1946.

[13] M. Hillert, "Pressure Induced Diffusion and Deformation During Precipitation, Especially Graphitization," *Jernkont. Ann*, vol. 141, pp. 157–181, 1957.

[14] M. Mantina, Y. Wang, L. Q. Chen, Z. K. Liu, and C. Wolverton, "First principles impurity diffusion coefficients," *Acta Materialia*, vol. 57, no. 14, pp. 4102–4108, 2009.

[15] S. . Kang and C. Laird, "Precipitation in thin foils of Al-4 wt.% Cu alloy—II. Growth kinetics of θ precipitates," *Acta Metallurgica*, vol. 23, no. 1, pp. 35–49, Jan. 1975.

[16] I. M. Lifshitz and V. V. Slyozov, “The kinetics of precipitation from supersaturated solid solutions,” *Journal of Physics and Chemistry of Solids*, vol. 19, no. 1–2, pp. 35–50, Apr. 1961.
[17] C. Wagner, “Theorie der Alterung von Niederschlägen durch Umlösen (Ostwald-Reifung),” *Zeitschrift für Elektrochemie, Berichte der Bunsengesellschaft für physikalische Chemie*, vol. 65, no. 7-8, pp. 581–591, 1961.
[18] A. . Ardell, “The effect of volume fraction on particle coarsening: theoretical considerations,” *Acta Metallurgica*, vol. 20, no. 1, pp. 61–71, Jan. 1972.
[19] C. K. L. Davies, P. Nash, and R. N. Stevens, “The effect of volume fraction of precipitate on ostwald ripening,” *Acta Metallurgica*, vol. 28, no. 2, pp. 179–189, Feb. 1980.
[20] Y. Enomoto, M. Tokuyama, and K. Kawasaki, “Finite volume fraction effects on Ostwald ripening,” *Acta Metallurgica*, vol. 34, no. 11, pp. 2119–2128, Nov. 1986.
[21] J. D. Boyd and R. B. Nicholson, “The coarsening behaviour of θ″ and θ′ precipitates in two Al-Cu alloys,” *Acta Metallurgica*, vol. 19, no. 12, pp. 1379–1391, Dec. 1971.
[22] P. Merle and F. Fouquet, “Coarsening of θ′ plates in al-cu alloys—I. experimental determination of mechanisms,” *Acta Metallurgica*, vol. 29, no. 12, pp. 1919–1927, Dec. 1981.
[23] P. W. Voorhees and M. E. Glicksman, “Solution to the multi-particle diffusion problem with applications to ostwald ripening—II. Computer simulations,” *Acta Metallurgica*, vol. 32, no. 11, pp. 2013–2030, Nov. 1984.
[24] H. I. Aaronson, “Discussion of ‘on the growth kinetics of plate-shaped precipitates in aluminum-copper and aluminum-gold alloys’ by YH Chen and RD Doherty,” *Scripta Metallurgica*, vol. 11, no. 9, pp. 731–732, 1977.
[25] S. . Kang and C. Laird, “Precipitation in thin foils of Al-4 WT.% Cu alloy—I. Morphology, crystallography and interfacial structure of θ precipitates,” *Acta Metallurgica*, vol. 22, no. 12, pp. 1481–1495, Dec. 1974.
[26] E. Orowan, “Symposium on Internal Stresses in Metals and Alloys,” *Institute of Metals, London*, vol. 451, 1948.
[27] J. F. Nie, B. C. Muddle, and I. J. Polmear, “The Effect of Precipitate Shape and Orientation on Dispersion Strengthening in High Strength Aluminium Alloys,” *Materials Science Forum*, vol. 217–222, pp. 1257–1262, 1996.
[28] J. F. Nie and B. C. Muddle, “Microstructural design of high-strength aluminum alloys,” *Journal of Phase Equilibria*, vol. 19, no. 6, pp. 543–551, 1998.
[29] C. Calabrese and C. Laird, “Cyclic stress-strain response of two-phase alloys Part II. Particles not penetrated by dislocations,” *Materials Science and Engineering*, vol. 13, no. 2, pp. 159–174, 1974.
[30] J. da Costa Teixeira, L. Bourgeois, C. W. Sinclair, and C. R. Hutchinson, “The effect of shear-resistant, plate-shaped precipitates on the work hardening of Al alloys: Towards a prediction of the strength-elongation correlation,” *Acta Materialia*, vol. 57, no. 20, pp. 6075–6089, 2009.
[31] K. G. Russell and M. . Ashby, “Slip in aluminum crystals containing strong, plate-like particles,” *Acta Metallurgica*, vol. 18, no. 8, pp. 891–901, Aug. 1970.
[32] J. F. Nie and B. C. Muddle, “Strengthening of an Al–Cu–Sn alloy by deformation-resistant precipitate plates,” *Acta Materialia*, vol. 56, no. 14, pp. 3490–3501, 2008.
[33] S. P. Ringer and K. Hono, “Microstructural Evolution and Age Hardening in Aluminium Alloys,” *Materials Characterization*, vol. 44, no. 1–2, pp. 101–131, Jan. 2000.

[34] B. C. Muddle and J. F. Nie, “Nucleation-mediated Structural Refinement and Aluminium Alloy Design,” *Materials Science Forum*, vol. 519/521, pp. 191–196, 2006.
[35] B. K. Park, V. Greenhut, G. Luetjering, and S. Weissman, “Dependence of Fatigue Life and Flow Stress on the Microstructure of Precipitation-Hardened Al-Cu Alloys.” 1970.
[36] R. L. Fleischer, “Substitutional solutes in AlRu—I. Effects of solute on moduli, lattice parameters and vacancy production,” *Acta Metallurgica et Materialia*, vol. 41, no. 3, pp. 863–869, Mar. 1993.
[37] M. F. Ashby, “The deformation of plastically non-homogeneous materials,” *Philosophical Magazine*, vol. 21, no. 170, pp. 399–424, Feb. 1970.
[38] L. M. Brown and W. M. Stobbs, “The work-hardening of copper-silica,” *Philosophical Magazine*, vol. 23, no. 185, pp. 1201–1233, May 1971.
[39] V. Andrade *et al.*, “Nanoscale 3D imaging at the advanced photon source,” *SPIE Newsroom*, 2016.
[40] F. Roters, P. Eisenlohr, L. Hantcherli, D. D. Tjahjanto, T. R. Bieler, and D. Raabe, “Overview of constitutive laws, kinematics, homogenization and multiscale methods in crystal plasticity finite-element modeling: Theory, experiments, applications,” *Acta Materialia*, vol. 58, no. 4, pp. 1152–1211, 2010.
[41] P. Eisenlohr, M. Diehl, R. A. Lebensohn, and F. Roters, “A spectral method solution to crystal elasto-viscoplasticity at finite strains,” *International Journal of Plasticity*, vol. 46, pp. 37–53, Jul. 2013.
[42] R. J. Asaro and A. Needleman, “Overview no. 42 Texture development and strain hardening in rate dependent polycrystals,” *Acta Metallurgica*, vol. 33, no. 6, pp. 923–953, Jun. 1985.
[43] S. G. I. Taylor, *Plastic Strain in metals*. 1938.
[44] X. Wu, S. R. Kalidindi, C. Necker, and A. A. Salem, “Prediction of crystallographic texture evolution and anisotropic stress–strain curves during large plastic strains in high purity α-titanium using a Taylor-type crystal plasticity model,” *Acta Materialia*, vol. 55, no. 2, pp. 423–432, Jan. 2007.
[45] A. A. Salem, S. R. Kalidindi, and S. L. Semiatin, “Strain hardening due to deformation twinning in α-titanium: Constitutive relations and crystal-plasticity modeling,” *Acta Materialia*, vol. 53, no. 12, pp. 3495–3502, Jul. 2005.
[46] S. R. Kalidindi, “Modeling anisotropic strain hardening and deformation textures in low stacking fault energy fcc metals,” *International Journal of Plasticity*, vol. 17, no. 6, pp. 837–860, Jul. 2001.
[47] F. Apostol and Y. Mishin, “Interatomic potential for the Al-Cu system,” *Phys. Rev. B*, vol. 83, no. 5, p. 054116, Feb. 2011.
[48] Q. Zhou, J. Wang, A. Misra, P. Huang, F. Wang, and K. Xu, “Atomistic study of fundamental character and motion of dislocations in intermetallic Al2Cu,” *International Journal of Plasticity*, vol. 87, pp. 100–113, Dec. 2016.
[49] W. Zhou, L. Liu, B. Li, Q. Song, and P. Wu, “Structural, Elastic, and Electronic Properties of Al-Cu Intermetallics from First-Principles Calculations,” *Journal of Elec Materi*, vol. 38, no. 2, pp. 356–364, Feb. 2009.